Polysilicon Microchips Functionalized with Bipyridinium-based Cyclophanes for a Highly Efficient Cytotoxicity in Cancerous Cells

Journal:	*ACS Nano*
Manuscript ID	nn-2021-08090a.R2
Manuscript Type:	Article
Date Submitted by the Author:	n/a
Complete List of Authors:	Limón, David; Northwestern University, Department of Chemistry Hornick, Jessica; Northwestern University, Molecular Biosciences Cai, Kang; Northwestern University, Department of Chemistry Beldjoudi, Yassine; Northwestern University, Department of Chemistry Duch, Marta; Instituto de Microelectrónica de Barcelona Plaza, Jose A; Instituto de Microelectrónica de Barcelona, Micro and Nanosystems Pérez-García, Lluïsa; Universitat de Barcelona, Pharmacology and Therapeutical Chemistry, Faculty of Pharmacy and Food Science Stoddart, J. Fraser; Northwestern University, Department of Chemistry

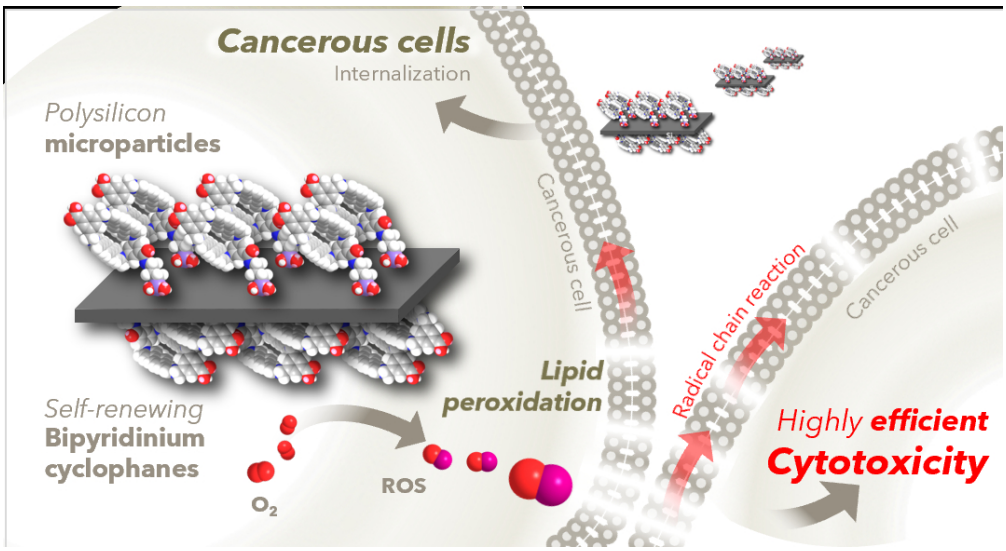

Self-renewing bipyridinium-functionalized microparticles internalize in cancerous cells and induce lipid peroxidation in cell membranes, leading to a highly efficient cytotoxicity.

Polysilicon Microchips Functionalized with Bipyridinium-based Cyclophanes for a Highly Efficient Cytotoxicity in Cancerous Cells

David Limón[a,b,c] *, Jessica E. Hornick[d], Kang Cai[a], Yassine Beldjoudi[a], Marta Duch[e], José A. Plaza[e], Lluïsa Pérez-García [b,c], J. Fraser Stoddart[a,f,g,h] *

[a]Department of Chemistry, Northwestern University, 60208, Evanston, Illinois, United States.
[b]Department of Pharmacology, Toxicology, and Therapeutic Chemistry, Faculty of Pharmacy and Food Science, University of Barcelona, 08028, Barcelona, Spain.
[c]Institute of Nanoscience and Nanotechnology, University of Barcelona (IN2UB), 08028, Barcelona, Spain.
[d]Department of Molecular Biosciences, Northwestern University, 60208, Evanston, Illinois, United States.
[e]Institute of Microelectronics of Barcelona IMB-CNM (CSIC), 08193, Barcelona, Spain.
[f]School of Chemistry, University of New South Wales, Kensington NSW 2033, Sydney, Australia
[g]Stoddart Institute of Molecular Science, Department of Chemistry, Zhejiang University, 311418, Hangzhou, China
[h]ZJU-Hangzhou Global Scientific and Technological Innovation Center, 311215, Hangzhou, China
Email: davidlimon@ub.edu; stoddart@northwestern.edu

Abstract

The use of micrometric-sized vehicles could greatly improve selectivity of cytotoxic compounds as their lack of self-diffusion could maximize their retention in tissues. We have used polysilicon microparticles (**SiμP**) to conjugate bipyridinium-based compounds, able to induce cytotoxicity under regular intracellular conditions. Homogeneous functionalization in suspension was achieved, where the open chain structure exhibits a more dense packing than cyclic analogues. The microparticles internalized induce high *cytotoxicity per particle* in cancerous Hela cells, and the less densely packed functionalization using cyclophanes promote higher *cytotoxicity per bipy* than with open chain analogues. The self-renewing ability of the particles and their proximity to cell membranes may account for increased lipid peroxidation, achieving toxicity at much lower concentrations than in solution, and proving these microchips as a promising platform for inducing highly efficient cytotoxicity in cancerous cells.

Keywords: polysilicon microparticles, bipyridinium, Hela cells, cancer, lipid peroxidation, cytotoxicity.

Highly cytotoxic compounds are essential in cancer chemotherapy. Chemotherapeutic drugs used in the clinic typically inhibit mitosis in cancerous cells, by either binding to DNA (*e.g.* doxorubicin),[1] inhibiting the production of DNA base pairs (*e.g.* methotrexate),[2] inhibiting topoisomerase enzyme which untangles DNA for its replication (*e.g.* topotecan),[3] binding to protein kinase receptors (*e.g.* imatinib),[4] or inhibiting the functional assembly of microtubules (*e.g.* paclitaxel),[5] all of which result in cell death. After oral or intravenous administration, however, their circulation in blood, extravasation, further diffusion across healthy tissues, and lack of selectivity for cancerous cells leads to cytotoxicity in healthy tissues as well, inducing side effects in patients.[6–9]

Some strategies for focalizing the cytotoxic effects within tumors and reducing side effects have been developed. Photodynamic therapy (PDT), which relies on the generation of reactive oxygen species (ROS) in cells upon

irradiation of a previously administered photosensitizer, permits the focalization of the irradiation, but the distribution of the photosensitizers across other tissues lead to side effects after sun exposure.[10]

Intratumoral chemotherapy (ITC), another strategy that has recently gained interest, relies on the direct injection of chemotherapeutic drugs within a tumor. It permits controlling the initial amount and localization of the drug administered, assisted by relatively simple techniques (*e.g.* ultrasound imaging). However, the injected drugs can also diffuse to surrounding tissues and be reabsorbed into the systemic circulation.[10]

A widely used strategy is the encapsulation of chemotherapeutic drugs into nanocarriers (*e.g.* vesicles, liposomes, or nanoparticles). According to the Enhanced Permeability and Retention (EPR) effect, the larger size of nanocarriers as compared to free drugs in solution promotes higher extravasation and retention in solid tumors, where the vasculature is leaky and the lymphatic vessels constricted.[11–14] Nonetheless, the efficiency of the EPR effect to target tumors has been recently questioned because, as although a higher extravasation can occur in the tumor area, the densely packed cancerous cells may keep the nanocarriers in the periphery of the tumor,[15] with only negligible amounts reaching the cells.[16,17] Another beneficial aspect of nanocarriers is their decreased Brownian motion as compared to molecules in solution, according to the Stokes-Einstein equation.[18] Therefore, once the nanocarriers are located within a tumor, they show decreased diffusion to surrounding healthy tissues. Recent studies demonstrate that the dense cell packing reduces the mobility of the particles in the medium much more than predicted by theory, where the self-diffusion coefficient across cells is exponentially decreased by the square of the radius of the particles.[19] Many aspects influence this decreased diffusion, including a higher contact area with cell membranes,[20] hydrophobicity of the cell membranes,[21] cell uptake,[20] positive charges on the particles surface,[22] or higher rates of sedimentation.[23] However, the self-diffusion is not negligible; in fact, nanoparticles can even diffuse through the tissues with barrier function, for example, nanoparticles can be used as transdermal delivery systems.[15,24–27] As well, chemotherapeutic drugs are typically nanoencapsulated by non-covalent bonds, such as electrostatic or hydrophobic interactions, which could result in leakage of the drugs before reaching the tumor, or their diffusion from the tumor to surrounding tissues. Examples of this phenomenon include doxorubicin-containing liposomes (Doxil®), which commonly induce dermatitis, flushing, and shortness of breath, and paclitaxel-containing liposomes (Abraxane®), which increase the cost of treatment as higher doses are required for a similar efficacy.[14]

Instead, the use of micrometric-sized particles would provide considerable advantages, such as their negligible self-diffusion coefficients in suspension and especially in tissues,[18,19,28] improving their retention in the site of administration along time. Silicon microparticles can be fabricated using photolithographic techniques or milling,[29,30] and due to their biocompatibility they have been used for drug delivery applications,[31,32] but encapsulating the drugs non-covalently in the nanoporous material. We have shown that micrometric-sized particles of different materials, shapes, and sizes can be fabricated using microelectronic-based techniques,[33] achieving extremely low polydispersity as compared to microparticles chemically synthesized. They can interact with living cells, working as intracellular pH sensors,[34] as micrometric tags for real-time tracking of cells,[35–37] or other applications. Among the different types of particles, hexahedral polysilicon (3 x 3 x 0.5 μm) microparticles (**SiμP**) represent a simple platform for immobilization of compounds with biomedical interest, as they can be easily observed even under brightfield microscopy, are relatively innocuous, and can be internalized into cells without reaching the nucleus.[37–41] Also, the compounds conjugated to the particles can maintain their physicochemical properties; for example, porphyrins immobilized onto **SiμP** show fluorescence equivalent to that in solution and can generate singlet oxygen in PDT.[42]

On the other hand, bipyridinium-derived compounds have wide interest for their ability to work as components of molecular machines, as π-electron-deficient bipyridinium moieties interact with π-electron-rich donor compounds, producing a host-guest interaction that can be controlled under external stimuli. The range of different architectures of bipyridinium compounds permits the template-guided synthesis of mechanically

interlocked molecules such as catenanes, rotaxanes, or pseudorotaxanes, which can be used as molecular switches,[43,44] artificial molecular muscles,[45] among others. Moreover, bipyridinium compounds show interesting optical properties that may be useful in for imaging applications.[46–48] However, the use of compounds bearing bipyridinium moieties for biomedical applications remains limited because of their intrinsic toxicity. Instead, the 1,1′-dimethyl-4,4′-dipyridinium dication, commonly known as methyl viologen (**1**) (Figure 1, A), has been used extensively as an herbicide.[49] The cytotoxicity of bipyridinium moieties is due to their easy reduction to the radical cation entity under mild intracellular conditions, such as the presence of NADPH catalyzed by NADPH-cytochrome c reductase. In presence of dissolved oxygen, the radical cation is oxidized again regenerating the bipyridinium moiety. Upon oxidation, superoxide radical anion is formed and transformed into other oxygen radicals, which attack unsaturated lipids of the cell membrane triggering lipid peroxidation, a radical chain reaction that eventually induces increased membrane fluidity, membrane integrity loss, and cell death.[49–51] Although this toxicity is also non-selective for cancerous cells, it could be revisited for biomedical purposes such as the treatment of cancer, as it is independent on nucleus internalization, making it more efficient than other chemotherapeutic drugs. The cytotoxic potential of bipyridinium on cancerous cells has been studied in solution, observing that the length of the alkyl chain substituents has an important influence on their cytotoxicity;[52] nonetheless, strategies for focalizing their cytotoxic effects still need to be found. Bipyridinium-derived compounds have been conjugated onto nanoparticles, mainly for electrochemical sensing,[53,54] or as gatekeepers of drug-loaded systems,[55,56] but not for this purpose.

Therefore, **SiμP** could be functionalized with compounds bearing bipyridinium moieties, as a platform that could potentially improve the spatial focalization of the cytotoxic effects in tissues. The microparticles could be directly injected with control over the number and location of particles dosed. The cytotoxic effects could be focalized due to the negligible diffusion of the microparticles and the covalent conjugation of the drugs that prevents their leakage and further diffusion in solution. For this reason, compounds **1**, **2**, and **3** (Figure 1, A) were selected for having bipyridinium moieties in different number and arrangement, and a strategy was designed to immobilize them onto **SiμP**. The functionalization was first optimized on macroscopic wafers patterned with polysilicon microparticles (Figure 1, B), with the purpose of controlling the functionalization along different stages using parameters such as the hydrophobicity, the fluorescence, or the atomic content. Once the functionalization protocol was optimized, the protocol was adapted to functionalize the microparticles in suspension (Figure 1, C). The ability of the unfunctionalized and functionalized particles to be internalized in cancerous Hela cells was observed, and their ability to induce cell death was evaluated using confocal fluorescence microscopy, showing the great potential of **SiμP** functionalized with bipyridinium-containing compounds for inducing highly efficient cytotoxic effects in cancerous cells.

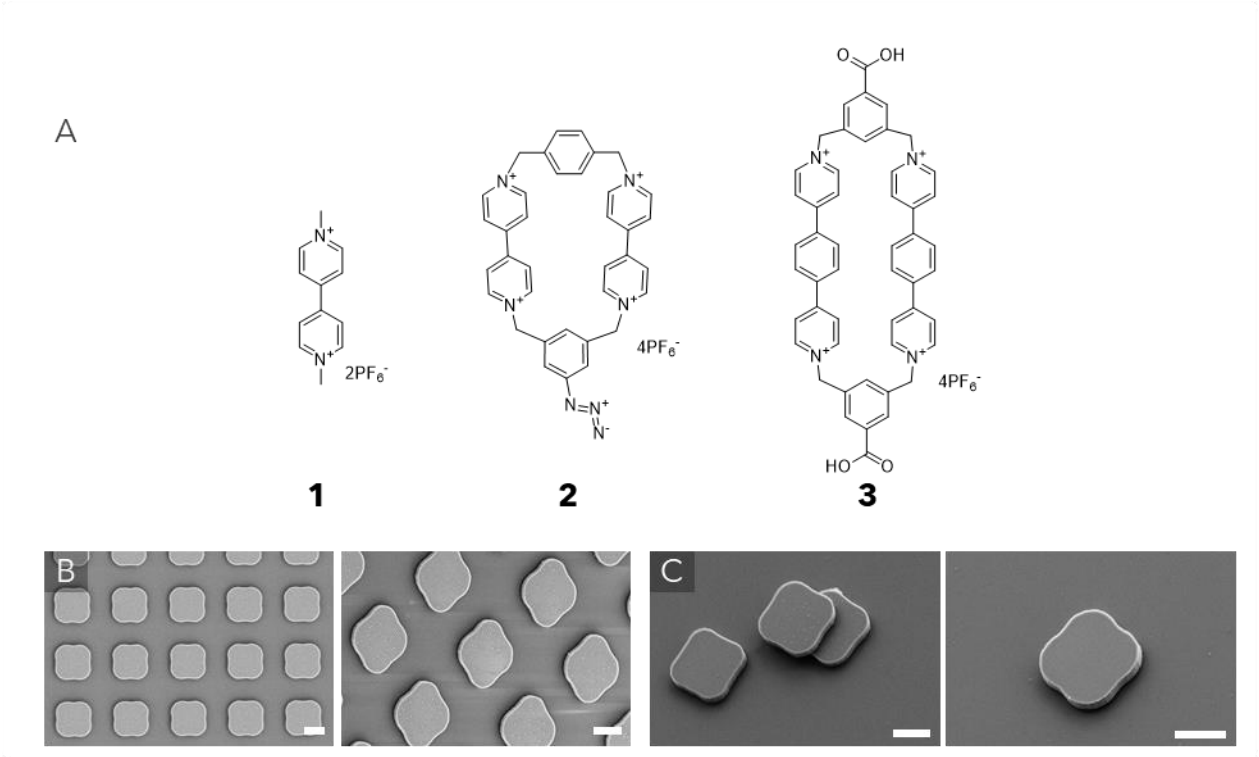

*Figure 1. (A) Chemical structures of compounds immobilized (**1**, **2**, and **3**). Compound **1** bears one bipyridinium moiety (open chain), whereas compounds **2** and **3** bear two bipyridinium moieties (cyclic structure). Compound **3** bears bipyridinium moieties extended by p-phenylene spacers. (B) SEM images of polysilicon microparticles fabricated onto a silicon oxide wafer. (C) SEM images of polysilicon microparticles once released in suspension (**SiμP**). Scale bar represents 2 μm.*

Results

Design of the system

With the aim of designing a system that could improve the localization of cytotoxic effects in chemotherapy, polysilicon microparticles (**SiμP**) were chosen for their biocompatibility and their potential to be chemically functionalized with cytotoxic compounds, their negligible diffusion, and their fast sedimentation. According to their easy internalization and localization within the cytoplasm, the compounds conjugated should display cytotoxicity through mechanisms different than the direct binding to DNA, as is the case of ROS generation. To this end, bipyridinium-containing compounds are ideal because they can be reversibly reduced under mild biological conditions and generate ROS.[50,51] Moreover, the overall number and arrangement of bipyridinium (bipy) units in the system could have an influence on the efficacy. For this reason, compounds **1**, **2**, and **3** (Figure 1, A) were selected to be conjugated to the **SiμP**, as **1** has been widely used and bears one bipy unit, whereas **2** and **3** both have two bipy units each in a macrocyclic structure, permitting a comparison between the macrocyclic *versus* the open-chain structures. In addition, **3** bears the bipyridinium moieties extended by *p*-phenylene groups, permitting a comparison between the extended *versus* the non-extended structures. Compound **2**, a structural analog of the widely-known *bluebox*,[43] was designed to incorporate an azide terminal group, used for its conjugation onto the particles, whereas compound **3** bears carboxylic acid groups for its conjugation.

The ability of the three selected compounds (**1**, **2**, and **3**) to be reversibly reduced in solution under mild conditions was confirmed using Differential Pulse Voltammetry (DPV) (Figure 2, A).

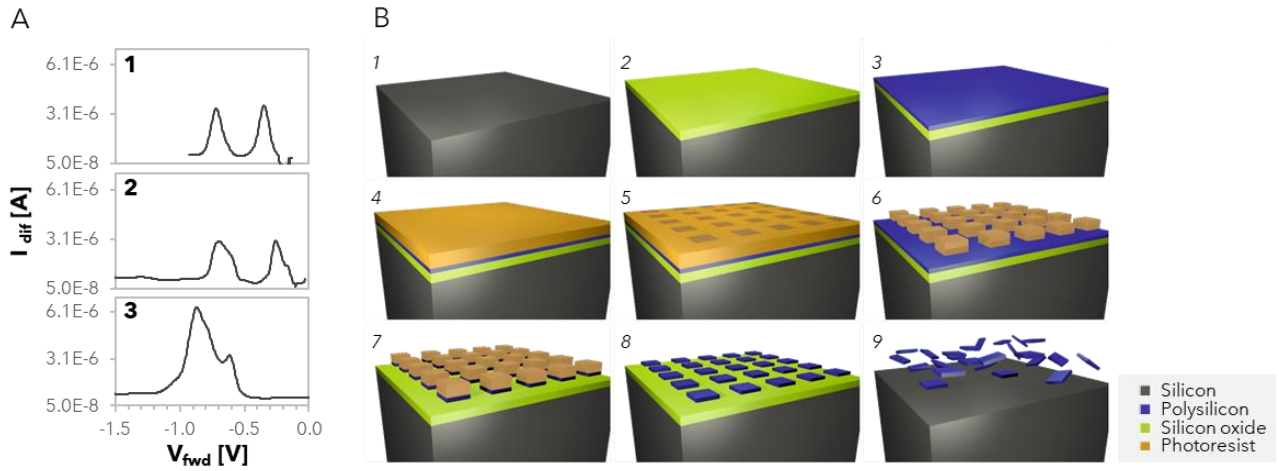

Figure 2. A) Differential Pulse Voltammograms of compounds ***1*** *(top),* ***2*** *(middle), and* ***3*** *(bottom) in DMF solution (1 mg per 3 mL). B) Schematic representation of* ***SiμP*** *fabrication. (1) Silicon wafer. (2) A silicon oxide layer is grown as sacrificial layer. (3) A polysilicon layer is deposited as structural layer. (4-5) A photoresist layer is spun and exposed to light. (6) Photoresist after developer. (7) Dry etching of the exposed polysilicon layer. (8) Photoresist removal. (9) Sacrificial etching of the silicon oxide layer to release the chips.*

The voltammogram for **1** (top) shows two oxidation-reduction peaks at −0.33 and −0.71 V, corresponding to two possible redox transitions, the first one occurring from the dicationic form to the radical cation entity, and the second one occurring from the radical cation to the neutral entity. As the structure of **2** (middle) contains two equivalent bipyridinium moieties, also two peaks are observed in its voltammogram at −0.25 V and −0.67 V, corresponding to the same redox transitions. In contrast, **3** (bottom) showed two peaks that are partially overlapped, occurring at −0.60 and −0.88 V, respectively. The results also show that the compound presenting the first redox transition (to the radical cation) at the potential closest to zero is **2** (−0.25 V), occurring at slightly higher values than that of **1** (−0.3 V), and showing values very similar to those of its isomer *bluebox,*[57] whereas the first reduction in **3** occurs at a more negative potential (−0.60 V), indicating that the extended bipyridinium moieties lead to a more difficult transition to the radical cation moiety. Although the use of DMF might lead to small differences in the redox potential as compared to biological media, the ability of compound **1** to be intracellularly reduced by NADPH catalyzed by NADPH-cytochrome c dehydrogenase, and re-oxidized in presence of oxygen is well documented,[50,51] for which the comparable potentials between the three compounds in DMF indicate that all of them can be intracellularly reduced. Nonetheless, although this finding could initially predict that compounds **2** and **1** could induce higher ROS generation in cells as compared to **3** when administered in solution, the covalent immobilization of these compounds on the surface of the microparticles could influence their redox transitions and thus their ability to generate ROS.

Polysilicon microparticles (**SiμP**) were fabricated as shown in Figure 1, B .[41,42] Briefly, a 1-μm thick *p*-type silicon wafer with a 100-mm diameter was used as a starting substrate (1). A silicon oxide layer was grown as a sacrificial layer (2). Next, a 500 nm polysilicon layer was deposited on top as a structural layer (3). By using microelectronic fabrication techniques as lithography and dry etching, the **SiμP** were patterned (4-8). The patterned particles have a cuboid shape with lateral dimensions defined by the photolithographic processes and their thickness defined by the thickness of the previously deposited structural layer (3 x 3 x 0.5 μm^3). Lastly, the particles were released from the substrate by a sacrificial etching of the sacrificial silicon oxide layer using a vapor of 50 % hydrogen fluoride (9), and then suspended and collected in ethanol in Eppendorf tubes for their posterior chemical functionalization.

The functionalization was first optimized using macroscopic silicon oxide wafers with the polysilicon microparticles on top (Figure 1, B; Figure 2, B 8), as it permits an easier manipulation of the material as well as the characterization of the properties of the surface such as hydrophobicity, fluorescence, or elemental composition. Once the protocol is optimized, the reaction setup can be adapted to functionalize the polysilicon microparticles in suspension. Therefore, the chemical strategy was designed to overcome the future limitations of microparticle functionalization, such as the limited range of temperatures for using plastic microtubes, or the use of solvents that permit suspending the microparticles under vortex but also sedimenting them under centrifugation during washes. In general, **SiμP** are more easily suspended in water than in organic solvents (*e.g.* acetone, ethanol, isopropanol), making their sedimentation difficult and leading to considerable particle losses. For this reason, water was avoided whenever possible along the functionalization.

Figure 3 (A-C) shows the optimized strategy for obtaining silicon wafers functionalized with the three different bipyridinium-containing compounds, **1** (**Si—1**) (A), **2** (**Si—2**) (B), or **3** (**Si—3**) (C), where the different functionalization steps followed are numbered under each structure (*functionalization stages*) for the purpose of clarity. According to this strategy, the counter anions of the bipyridinium moieties formed upon conjugation of the compounds are hexafluorophosphate anions in the case of **Si—2** and **Si—3**, and bromide and iodide in the case of **Si—1**. Although it is well known that the counter anion has an influence on the solubility of bipyridinium compounds and may affect their reduction potential, the immersion of the functionalized microparticles in a biological medium would likely result in the exchange of the counter anions for those present in the medium, such as phosphate or chloride, and for which the effect of the counter anion on the efficacy could be negligible. The three different self-assembled monolayers (SAMs) were designed to have similar thicknesses (the total length of the linker-bipyridinium compound is similar), for which the properties of the material and of the microparticles, as well as their efficacy, could be related to the number and arrangement of bipyridinium units. MM2 minimizations of the functionalized moieties in each type of particle were performed (See Supporting Information "MM2 calculations"), and ideal representations of the respective SAMs formed are shown in Figure 3 (D, E, and F, respectively). As it can be seen, the open chain structure of the moieties conjugated in **Si—1** permits a more densely packed SAM as compared to the cyclic structures in **Si—2** and **Si—3** , meaning that a higher number of molecules of **1** could be conjugated on the surface.

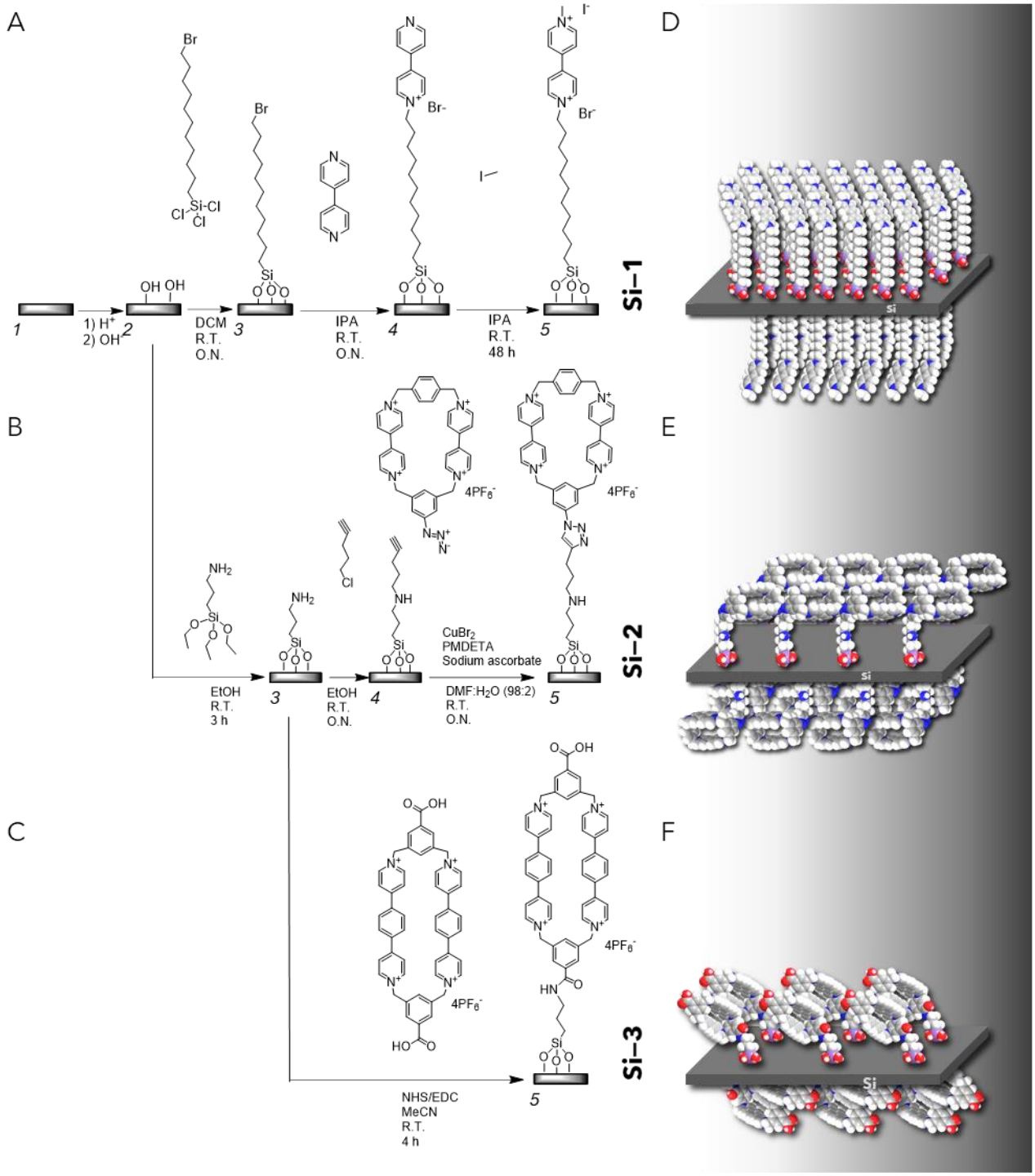

*Figure 3. (A-C) Functionalization strategy followed for obtaining silicon wafers functionalized with (A) **1** (**Si–1**), (B) **2** (**Si–2**), or (C) **3** (**Si–3**). Functionalization stages are displayed under each structure for the purpose of clarity. (D-F) Ideal models of functionalized silicon wafers (D) **Si–1** (E) **Si–2**, and (F) **Si–3** according to MM2 minimizations.*

Functionalization of silicon wafers

Wafers of ≈0.25 cm² were first washed with water and ethanol and were dried with a stream of nitrogen (stage 1). Subsequently, the wafers were activated using acid treatment followed by basic treatment (stage 2) to provide

the surface with hydroxyl groups. After activation, a suitable linker bearing a silane moiety was covalently attached to the hydroxyl groups on the surface (stage 3). This linker therefore acts as a spacer and provides a suitable functional group for further attachment of the bipyridinium compounds. Functionalization of wafer surfaces with methyl viologen (**Si—1**) (Figure 3, A), consists of the use of 11-bromoundecyl trichlorosilane as the linker (stage 3), which provides the surface with an alkyl bromide group, the subsequent conjugation of the 4,4'-bipyridine (stage 4), and the final installation of a methyl group using methyl iodide (stage 5). The functionalization with **2** (**Si—2**) is carried out by using APTES as the linker (stage 3), the conjugation of propargyl bromide as a secondary linker (stage 4), which provides the surface with a terminal alkyne group, and the final conjugation of compound **2** through a Cu(I)-catalyzed azide-alkyne cycloaddition (stage 5). Likewise, the functionalization with **3** (**Si—3**) entails the use of APTES as the linker (stage 3) providing the surface with terminal amino groups, and the final conjugation of the **3** using NHS/EDC coupling (stage 5). All reactions were performed at room temperature. After each reaction, the wafers were thoroughly washed with the solvent used in the reaction to remove excess reactants, then with acetone, and were finally dried with a stream of nitrogen before the next stage.

The functionalization was first assessed by performing contact angle measurements on the wafers, to determine their hydrophobicity upon each functionalization stage, as depicted in the Supporting Information (Table S 1). Silicon wafers without any functionalization (stage 1) show a contact angle of 46.2±5.2°, similar to previously reported results.[36,58] In contrast, the activation of the wafers performed by acid and basic treatment (stage 2) led to a significant decrease in the contact angle (23.5±4.3°), which is in accordance with the presence of hydroxyl groups on the surface. The further addition of the linker (stage 3) led in all cases to an increase in the contact angle, as the surface becomes more hydrophobic due to the presence of a hydrocarbon chain. The surface showing the highest contact angle in stage 3 is **Si—1** (96.4±2.0°), where the linker incorporates the longest alkyl chain (11 carbons), while the contact angle obtained when the linker is a 3-carbon chain and a final amino group (**Si—2** or **Si—3**) is 57.9±9.5°. Furthermore, the conjugation of a secondary linker (stage 4) resulted in a decrease in the contact angle. In the case of **Si—1** wafers, the conjugation of 4,4'-bipyridine in this stage implies the formation of one positive charge upon formation of one pyridinium moiety, leading to a more hydrophilic surface. Finally, in the three wafers studied (**Si—1**, **Si—2** and **Si—3**), stage 5 resulted in a further decrease in the contact angle as compared to the previous stage, in accordance with the positive charges of bipyridinium moieties that make the surface more hydrophilic. The lowest contact values observed correspond to **Si—2** and **Si—3** (22.7±5.2° and 25.6±3.4 °, respectively), where each conjugated compound have four positive charges, as opposed to **Si—1** having two positive charges. These results suggest successful functionalization along the different functionalization stages.

Quantification and homogeneity of the functionalization

The functionalization was assessed and quantified by studying the atomic content of the wafers along the different functionalization stages using XPS. Binding energy plots of the different elements analyzed in the different wafers (**Si—1**, **Si—2**, **Si—3**) can be found in the Supporting Information (Figure S 1 to Figure S 3, respectively). The atomic content of C1s, N1s, Br3d, I3d, P2p, and/or F1s relative to Si2p was calculated by dividing the atomic content of each element by the atomic content of Si2p. The relative atomic content calculated along the different functionalization stages can be seen in the Supporting Information (Table S 2 - Table S 4) and is shown in Figure 4.

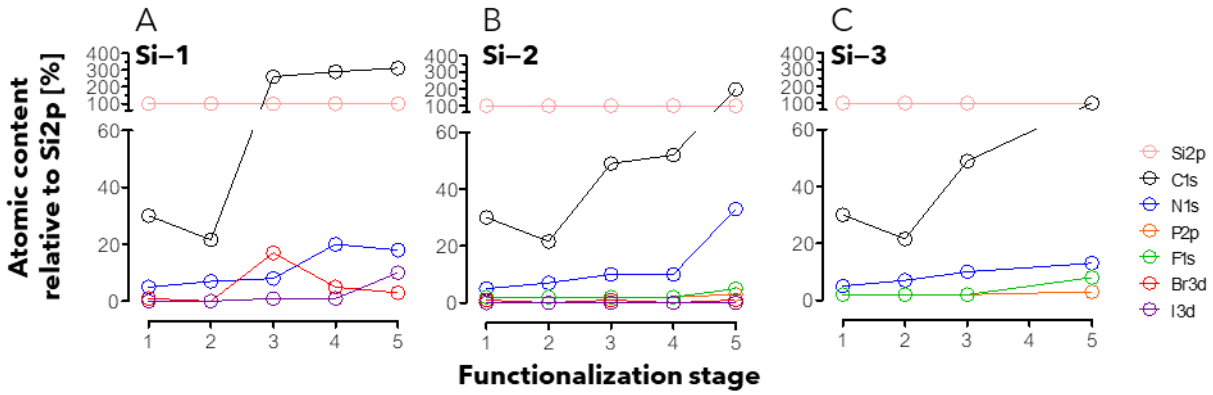

*Figure 4. Atomic content relative to Si2p along the different stages of functionalization (1 to 5) of silicon wafers: A) **Si–1**, B) Si–**2**, C) Si–**3**.*

The **Si–1** wafers (A) show subsequent increases in carbon content (with respect to Si2p) along the different stages, in accordance with the increasing carbon chain length on the surface. A drastic increase is especially seen in stage 3 (from 22 % to 260 % with respect to Si2p), corresponding to the conjugation of the 11-carbon linker. Likewise, a significant increase in bromine content (0 % to 17 %) is seen in stage 3, as it is covalently attached on the surface, in nitrogen content in stage 4 (from 8 % to 20 %), corresponding to the conjugation of 4,4'-bipyridine, and in iodine content in stage 5 (from 1 % to 10 %), showing the presence of the counter anion. Similarly, the functionalization of **Si–2** (Figure 4, B), shows a gradual increase in carbon content from stage 3, with a significant increase in stage 5 (from 52 % to 197 %), where the functionalization involves the highest number of carbon atoms attached. The gradual increase in nitrogen content along the stages also suggests a successful functionalization, especially considering that, during stage 5 (from 10 % to 33 %), the highest number of nitrogen atoms is functionalized on the surface. Furthermore, fluorine can be detected in stage 5 (from 2 % to 5 %), in accordance with the presence of PF_6^- counter anions. Likewise, **Si–3** wafers (Figure 4, C) show the presence of fluorine in stage 5 (from 2 % to 8 %) due to PF_6^- anions, while a gradual increase in carbon content was observed in stages 3 and 5.

The identity of the moieties functionalized on the surface was confirmed by calculating the ratio of N/C atomic content measured for each surface, as both are covalently bonded elements, and this ratio was compared to the theoretical ratio according to the chemical structure of each moiety (Table 1). The measured N/C ratios were similar to the theoretical N/C ratios for **Si–1** (0.06 vs 0.09, respectively), **Si–2** (0.17 vs. 0.18), and **Si–3** (0.13 vs. 0.09), suggesting functionalization in all cases.

*Table 1. Estimation of surface coverage [%] of functionalized silicon wafers (**Si–1**, **Si–2**, and **Si–3**) based on XPS analysis. The similarity of the measured N/C ratios to the theoretical N/C ratios suggests the correct identity of the conjugated moieties.*

	Si–1	**Si–2**	**Si–3**
Measured N1s content relative to Si2p [%]	17.6	32.6	12.8
Measured C1s content relative to Si2p [%]	311.3	197.4	100.1
Max theoretical C1s content relative to Si2p [%]	550	1100	1325
Surface coverage [%]	**57**	**18**	**8**
Measured N/C ratio	0.06	0.17	0.13
Theoretical N/C ratio	0.09	0.18	0.09
Estimated Si atoms functionalized per nm^2	41	13	5
Estimated moieties conjugated per nm^2	14	4	2
Estimated moieties conjugated per microparticle	3.25×10^8	1.03×10^8	4.34×10^7

In order to estimate the proportion of silicon atoms functionalized (surface coverage), the maximum theoretical atomic content (relative to Si2p) of each element was calculated assuming all the silicon atoms on the surface are functionalized forming a monolayer, and the measured atomic content from each sample was compared to the theoretical content. Also, according to the atomic radius of polycrystalline silicon (0.118 nm) (*ca.* 72 Si atoms per nm^2), the number of moieties functionalized per nm^2 was estimated (Table 1). According to the content of C1s, around 57 % of silicon atoms on the surface of **Si—1** wafers are functionalized (57 % surface coverage), meaning that up to 14 moieties of **1** could be immobilized per nm^2. In contrast, **Si—2** wafers show around 18 % surface coverage, meaning that up to 4 moieties of **2** could be conjugated per nm^2, and **Si—3** show around 8 % of surface coverage, meaning that up to 2 moieties of **3** could be conjugated per nm^2. These differences in surface coverage can be thus related to the structural differences, where the open chain structure in **Si—1** could form a tighter SAM containing a larger number of moieties, as observed in the representation based on MM2 minimizations (Figure 3, D), whereas the bigger macrocyclic structure of **Si—3** results in a lower number of moieties per surface area (Figure 3, F). The surface coverage values of N1s were similar to those of C1s, as both are covalently bonded, except for **Si—1** wafers, which had less coverage as compared to values of C1s (35 % vs 57 %), suggesting that some linkers on the monolayer do not react with 4,4'-bipyridine during stage 4 probably as a result of the tightly packed SAM. Similarly, the surface coverage of the elements of the counter anion (Br3d, I3d, F1s, and P2p) is considerably lower than C1s, suggesting that the counter anions might be exchanged during washes.

Moreover, the fluorescence of compound **3** was further used for assessing the functionalization of **Si—3** wafers using confocal fluorescence microscopy (See Supporting Information, Figure S 4). Homogeneous fluorescence was observed across the surface, suggesting the successful formation of a monolayer.

*Functionalization of **SiμP** in suspension*

Polysilicon microparticles (**SiμP**) previously collected in suspension were functionalized following a similar protocol to the one previously used for the silicon wafers (Figure 3) but adapted to the microparticles. For instance, reactions were carried out in Eppendorf tubes with typical reaction volumes of 100 μL. Sonication was used periodically (including at the beginning of each reaction) to induce homogeneous suspension of the microparticles, which was later maintained using vortex stirring. After each reaction, the microparticles were washed with centrifugation-resuspension cycles using the same solvent to remove excess reactants, then with acetone to remove the previous solvent, and the particles were finally dried using a stream of nitrogen. After the cleaning and activation step (performed in water) (stage 2), IPA and DMF were used as cosolvents to promote the sedimentation of the particles during the washes and decrease the particle loss. The functionalization strategy including the reaction conditions can be seen in the Supporting Information (Figure S 5). First, the microparticles with no previous treatment (**SiμP**) (stage 1) were subjected to a cleaning and activation step by using acid and basic treatment, providing the silicon surface with hydroxyl groups (stage 2). Activated microparticles were immersed in a solution of silane-bearing linkers that react with the hydroxyl groups of the **SiμP** (stage 3). Appropriate second linkers and/or compounds containing bipyridinium moieties were then covalently conjugated to the microparticles (stages 4 and 5).

As achieving homogeneous functionalization of microparticles in suspension remains a challenging task, the fluorescence of compound **3** was used to study the functionalization of **SiμP—3** microparticles using confocal fluorescence microscopy. Figure 5 (A) shows the fluorescence of **3** being in colocalization with the microparticles, while 3D-projections of transmission/fluorescence composites Figure 5 (B) show that the fluorescence is indeed localized on the surface of the microparticles, proving their functionalization. Furthermore, the homogeneity of the functionalization was studied by quantifying the fluorescence across four different sections of the microparticles (axes a - d), as shown in Figure 5 (C), and the data were plotted in an overlapped manner (Figure 5, D). The fluorescence intensity profiles for particles 1 and 2 display a constant intensity across the particle (according to the sensitivity of the technique), which shows they are homogeneously functionalized with **3**. In

contrast, intensity profiles for particle 3 show a decrease in the fluorescence in the central part of the plot, showing a lack of functionalization in the center of the particle. The mean fluorescence intensity from each axis was quantified (Figure 5, E) (n = 131 pixels measured), observing no differences between the four different axes (a - d) for each particle; however, different mean intensities can be observed when comparing between particles (Figure 5, F) (n = 524 pixels measured). For example, particle 2 shows around 20 % less intensity than particle 1, whereas particle 3 shows around 48 % less intensity than particle 1 ($P<0.0001$), evidencing a much more difficult chemical functionalization in suspension as compared to reactions taking place in solution. One-way Analysis of Variance (ANOVA) analysis with a Bonferroni's multiple comparison test can be seen in the Supporting Information (Table S 5).

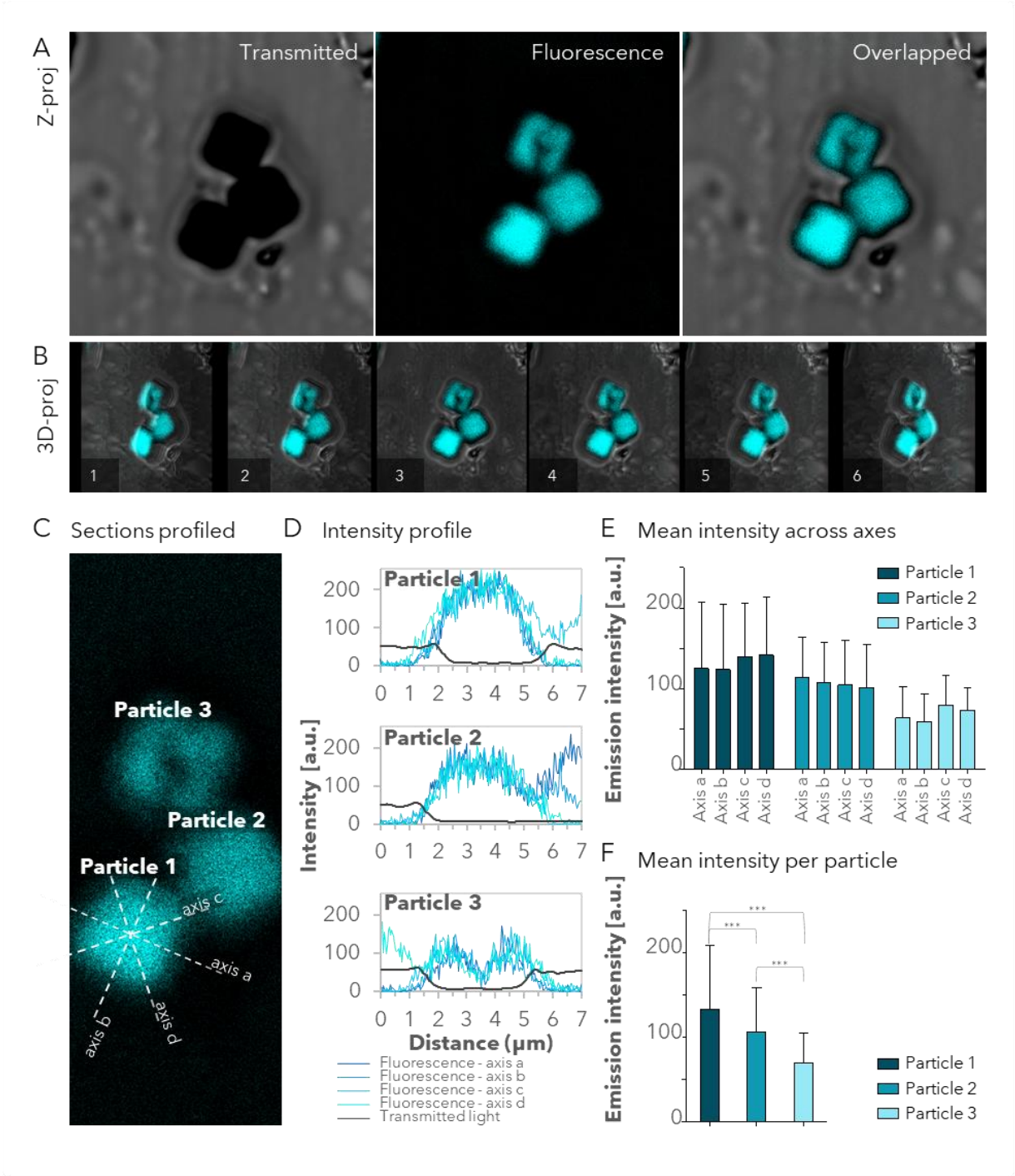

*Figure 5. Characterization of **SiµP–3** microparticles using confocal fluorescence microscopy. A) Z-projection images of representative **SiµP–3** microparticles observed under brightfield microscopy (left), fluorescence at λ ex = 405 nm and λ em = 420-600 nm (center), and overlapped images (right). B) 3D-projections of **SiµP–3** microparticles shown under different angles prove the localization of the fluorescence on the surface of the microparticles. C) The fluorescence intensity of the surface of the microparticles was analyzed across four different axes (a-d) in each particle as shown. D) Fluorescence intensity profiles along the axes were obtained using ImageJ and are plotted together with the transmitted light intensity profiles. E) The mean fluorescence intensity of each axis in each particle is plotted. Values represent Means ± SD (n = 131 pixels). F) The mean fluorescence intensity for each particle is plotted. Values represent Means ± SD (n = 524 pixels). ***Significant differences (P<0.0001).*

Particle count

In order to quantify the total number of particles recovered after functionalization, unfunctionalized **SiμP** and functionalized **SiμP−1**, **SiμP−2**, and **SiμP−3** particles were counted in transparent 96-well plates using a Lionheart FX automated microscope (see Supporting Information, Tables S 6 and S 7). The results show that an important number of particles are lost during functionalization depending on factors such as the number of reactions taking place, the number of washes performed after each reaction, and the type of solvents used. Unfunctionalized particles (**SiμP**), which are initially suspended in ethanol, are washed several times with water for removing ethanol completely before performing experiments with cells (stage 1). In the case of functionalized particles (**SiμP−1**, **SiμP−2** and **SiμP−3**), the activation step (stage 2) involves the use of a high proportion of water during the acid and basic treatments (while the resulting hydroxyl groups on their surface increase their polarity). Therefore, the highest fraction of unfunctionalized particles (≥90 %) are lost during washing (stage 1), whereas most functionalized particles are lost during activation (stage 2). After activation, functionalization of **SiμP−1** involves the use of less-polar organic solvents, permitting proper sedimentation and thus the highest particle recovery (95.1±13.9 %) with respect to washed unfunctionalized particles (**SiμP**). In contrast, the functionalization of **SiμP−2** and **SiμP−3** leads to recoveries of 33±4.1 % and 58±32 %, respectively, as a more polar solvent (ethanol) is used, while the functionalization involves 5 and 4 stages, respectively.

*Internalization of unfunctionalized microparticles (**SiμP**) in Hela cells*

The internalization of unfunctionalized microparticles (**SiμP**) in cancerous Hela cells was studied by adding different amounts of **SiμP** to the cells. Considering the impossibility to know the exact number of cells in wells before incubation due to great variability in biological systems, the approximate number of cells was estimated according to the confluency. For instance, cells grown to ≈80% confluency (ca. 100,000 cells per well) were treated with the microparticles, leading to approximate **SiμP:**cells ratios of 0.04:1, 0.08:1, 0.17:1, and 0.33:1. After 24-h incubation, the cells were observed under brightfield microscopy (See Supporting Information, Figure S 6). The results show that Hela cells can uptake one or more **SiμP** per cell, where a higher number of particles added results in a higher number of particles internalized per cell. The cells remained healthy according to continuation of division even at the highest dose tested (*ca.* **SiμP:**cells ratio 0.33:1). To further confirm the intracellular localization of the particles and eliminate the possibility of them being attached only to the membrane, confocal fluorescence microscopy was used. Cells were incubated for 24 h with 20 or 40 μL of suspended microparticles (**SiμP:**cells ratios 0.08:1 or 0.17:1, respectively) prior to observation. Figure 6 shows that the particles are localized in the same focal plane as actin fibers and nuclei, confirming the internalization into Hela cells, while no damage of the nuclear structure or the cytoskeletal framework is observed.

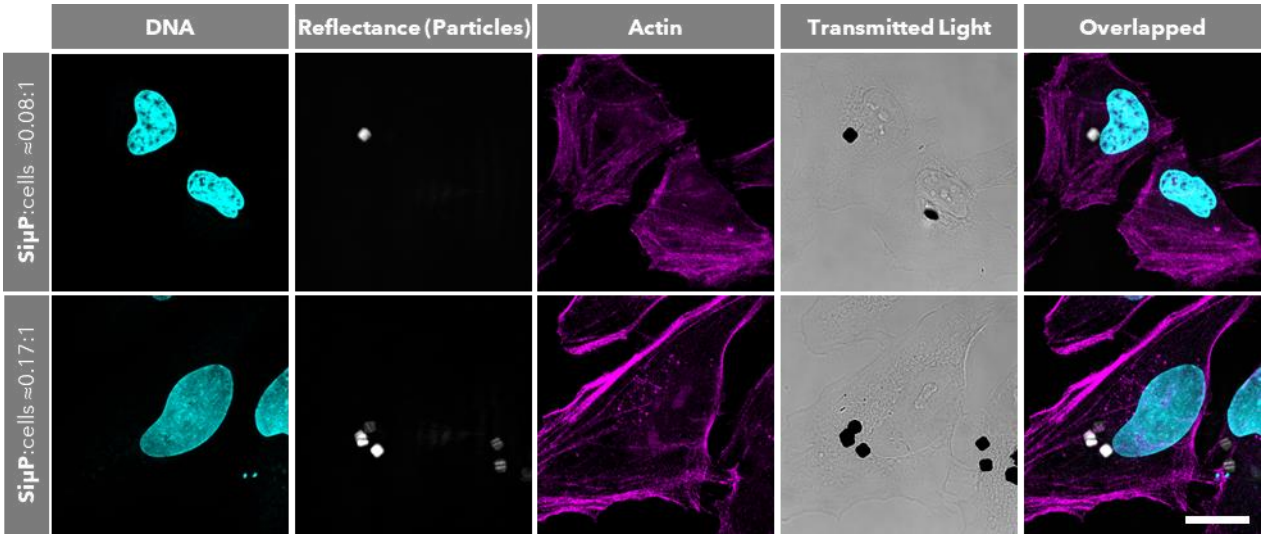

*Figure 6. Confocal fluorescence microscopy images of Hela cells after 24 h incubation with **SiμP** (unfunctionalized) at **SiμP**:cells ratios 0.08:1 (top) and 0.17:1 (bottom). Cells were stained with Phalloidin (targets filamentous actin) and Hoechst 33342 (targets DNA), and microparticles were observed in reflectance mode. Images were taken at 63x magnification. Scale bar is 20 μm.*

Cytotoxicity of functionalized microparticles in Hela cells

The cytotoxicity of functionalized (**SiμP—1**, **SiμP—2**, and **SiμP—3**) and unfunctionalized (**SiμP**) microparticles in Hela cells was studied at using confocal fluorescence microscopy. Microparticles in suspension (20 or 40 μL) were added to the cells, whereas PBS (20 or 40 μL) was added as a control (untreated), and cells were incubated for 24 h. Afterwards, cells were treated with live/dead staining, through which viable cells can be identified by their green fluorescence, as a result of the enzymatic activity of esterases, whereas dead cells are identified by red fluorescence, as a result of the binding of ethidium homodimer-1 to DNA, indicating loss of cell- and nuclear-membrane integrity. Samples were washed several times with PBS to remove non-internalized microparticles or fluorophore, as well as detached (nonviable) cells and were imaged at λ ex = 488 nm and λ em = 520-560 nm (green), or λ ex = 600 nm and λ em = 635-700 nm (red). In parallel, samples were imaged in brightfield mode to observe the microparticles and the morphology of cell membranes , while reflectance-mode data was acquired in some samples for easier visualization of the microparticles (shown in cyan). Figure 7 (A-J) shows the overlapped 3D-projections from the different focal planes acquired of the cells incubated with 20 μL (top) or 40 μL (bottom) of PBS (A-B) or a suspension of unfunctionalized (**SiμP**) (C-D) or functionalized **SiμP—1** (E-F), **SiμP—2** (G-H), or **SiμP—3** (I-J) microparticles. Pale blue arrows point to cells with particles internalized, while red arrows point to nonviable cells, either those with loss of cell membrane integrity, identified by a bumpy cell membrane, or those with loss of nuclear membrane integrity as well, identified by red fluorescence.

The *cell viability* [%] respect to the untreated sample was estimated according to the esterase activity of cells by quantifying the fluorescence intensity in the green channel. The *cell viability* was calculated following two complementary approaches. In the first approach, the fluorescence in the entire images was quantified, and values reflect the total esterase activity in the sample (Eq. 1). Thus, the total esterase activity is influenced by the number and size of cells (confluency) remaining as well as by the esterase activity of each cell, in a similar way as in other conventional methods in solution such as MTT.[59] In the second approach, the mean fluorescence in the cells is quantified, for which values are not influenced by the number and size of cells remaining, but they specifically reflect the esterase activity within cells (Eq. 2) (See Supporting Information, Figure S 7). Hence, the comparison of *cell viability* values using both approaches could provide information about the number and size of cells after treatment. The *cell viability* values observed after incubation with the microparticles were plotted as a function of

the **SiμP**:cells ratio of the sample (Figure 7, K), showing a dose-response relationship. In fact, values obtained using the total esterase activity (top) or the mean intracellular activity (bottom) were generally similar, showing a correlation between the intracellular esterase activity and cell confluency.

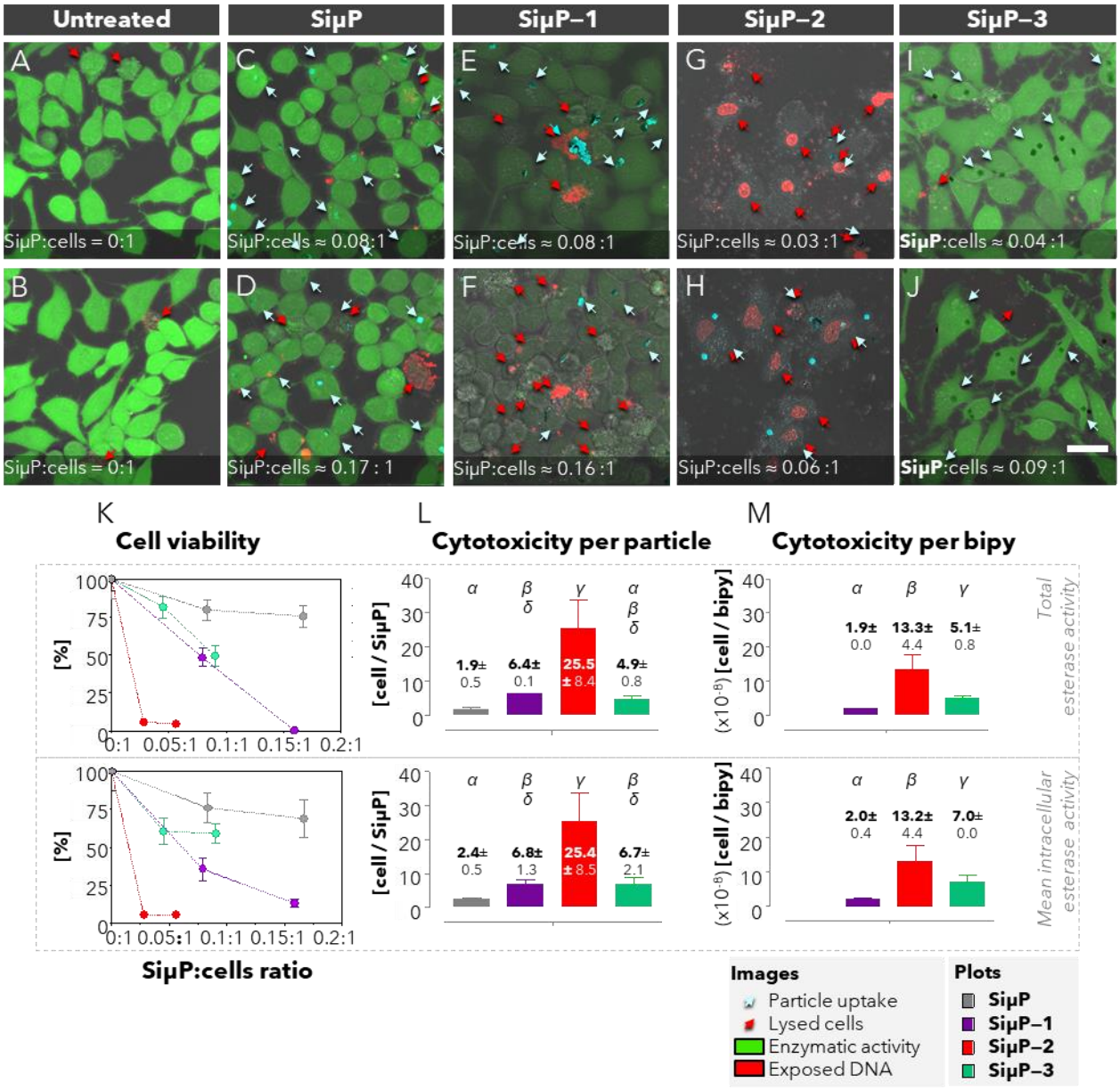

*Figure 7. A-J) Confocal fluorescence microscopy images of untreated[A-B] Hela cells or after 24-h incubation with either 20 μL (top) or 40 μL (bottom) unfunctionalized (**SiμP** [C-D]) or functionalized (**SiμP–1** [E-F], **SiμP–2** [G-H], or **SiμP–3** [I-J]) microparticles. Cells were washed with PBS after incubation to remove non-internalized microparticles as well as detached cells. Live/dead staining was applied to observe cells showing activity of intracellular esterases (green) and cells with cell and nuclear membrane integrity loss leading to DNA exposure (red). Sample was observed at λ ex = 488 nm and λ em = 520-560 nm (green), or λ ex = 600 nm and λ em = 635-700 nm (red). In parallel, samples were observed in brightfield mode to detect cell membranes and microparticles, while reflectance mode was acquired in some samples for easier visualization of the microparticles (shown in cyan). Images are displayed as projections of the different focal planes acquired. Pale blue arrows indicate the cells with particles internalized. Red arrows indicate nonviable or lysed cells as identified by their bumpy cell membrane morphology or DNA exposure. Scale bar is 30 μm. K) Viability of Hela cells upon 24 h incubation with different*

*SiμP:cell ratios of unfunctionalized (**SiμP**) and functionalized (**SiμP—1, SiμP—2,** or **SiμP—3**) microparticles. Cell viability is expressed as a percentage of total esterase activity in the sample (n=3) with respect to untreated cells (top) or mean intracellular esterase activity (n≥10) with respect to untreated cells (bottom) as measured by fluorescence intensity in the green channel. Values represent Means±SD. L). Cytotoxicity per particle [cell/**SiμP**] was obtained both according to the total esterase activity (top) or the mean intracellular esterase activity (bottom). M) Cytotoxicity per bipy [cell/bipy] was obtained according to the cytotoxicity per particle and total number of bipyridinium moieties conjugated per particle. Values represent Means±SD. Statistical significance: groups with sharing Greek letters show no significant differences (P>0.05), whereas groups with different letters are significantly different (P<0.05).*

Untreated Hela cells (Figure 7, A-B) are mostly healthy after incubation and show the highest esterase activity, while few dead cells are observed. In treated cells (Figure 7, C-J), most particles are internalized (pale blue arrows), but also some of them are observed outside the cells, and even some are embedded in the cell membrane, (*e.g.* Figure 7, D, center). Washing the cells several times before being imaged suggests that those particles outside the cells were most probably previously internalized, and were later released from the cells due to their loss of membrane integrity, for which it is possible that particles can be internalized in more than one cell during incubation.

The cells treated with unfunctionalized (**SiμP**) microparticles showed 76 % intracellular esterase activity and 80 % total esterase activity at a 0.08:1 **SiμP**:cells ratio, showing very mild toxicity in accordance to previous results.[37–40] In contrast, functionalized microparticles induce a higher toxicity in a dose-response relationship. Incubation with **SiμP—1** (E-F) results in a high proportion of cells with blebbing on the cell membrane, indicating start of apoptosis, and decreased green fluorescence, leading to 13.3 % mean intracellular esterase activity and 0.4 % total esterase activity at ≈0.16:1 **SiμP**:cells ratio. **SiμP—2** (G-H) shows the highest cytotoxic effect on Hela cells, where the particles are colocalized with cells but only unviable cells are observed even at the lowest **SiμP**:cells ratio (≈0.03:1) (G), and lead to only 5.9 % esterase activity, either intracellular or total. **SiμP—3** particles (I-J) show in some cases more than one particle internalized per cell, and although very few nonviable cells can be seen, 60.7 % intracellular esterase activity is observed at ≈0.03:1 **SiμP**:cells ratio, while 59.2 % at the highest (≈0.06:1) **SiμP**:cells ratio tested. Interestingly, incubation with **SiμP—3** within this range of **SiμP**:cells ratios did not show a dose-response decrease of the mean intracellular esterase activity, but did of the total esterase activity, evidencing a decrease in cell confluency.

Comparisons between the different particles were made by calculating the *cytotoxicity per particle* [cell/**SiμP**] (Eq. 3), an extrapolated value that considers the *cell viability* and the number of particles dosed (Figure 7, L). As the *cell viability* reflects the overall enzymatic activity of cells, the *cytotoxicity per particle* describes the overall damage to cell activity, and represents the equivalent number of cells that can die per particle administered if the remaining live cells maintained their esterase activity. For instance, unfunctionalized particles (**SiμP**) showed very low *cytotoxicity per particle* (1.9±0.5 cell/**SiμP** according to the total esterase activity). In contrast, all functionalized particles showed significantly higher toxicity . The highest *cytotoxicity per particle* was achieved by **SiμP—2**, (25.5±8.4 cell/**SiμP**), higher than the rest (P<0.001). On the other hand, **SiμP—3** shows a *cytotoxicity per particle* similar or slightly lower than **SiμP—1** (4.9±0.8 cell/**SiμP** vs 6.4±0.1, respectively). However, according to XPS measurements, **SiμP—1** particles show the highest surface coverage (ca. 14 moieties per nm^2), whereas **SiμP—3** show the lowest (ca. 2 moieties per nm^2). Taking in account these differences, the *cytotoxicity per bipy* [cell/bipy], was also calculated according to the total number of bipyridinium units conjugated per particle (Figure 7, M). In this line, there is a 2.7-fold higher *cytotoxicity per bipy* of **SiμP—3** as compared to **SiμP—1** evidencing the importance of both the number of bipyridinium units in the cells and their arrangement on the surface of the microparticles. The cyclic structure of **3** leads to a less densely packed layer of bipy units conjugated in **SiμP—3**, which could favor its interaction with dissolved oxygen to generate ROS, achieving more efficiency in ROS generation as compared to **SiμP—1**. On the other hand, **SiμP—2** show 2.6-fold higher *cytotoxicity per bipy* than **SiμP—3**. As both compounds **2** and **3** have a cyclic structure, the lower *cytotoxicity per bipy* of **SiμP—3** may be

influenced by the *p*-phenylene spacer in the bipyridinium units. According to DPV experiments, the redox transition of **3** occurs at a slightly lower potential than **1** or **2**, which may possibly account for a lower ROS generation and therefore lower cytotoxicity.

In solution, compounds bearing one bipyridinium moiety show IC_{50} values in cancerous cells ranging from 5.6 to 240 μM,[52] some of them showing even higher cytotoxicity than cisplatin (IC_{50} 15 to 142 μM). Thus, the equivalent concentration of compounds **1**, **2**, and **3** conjugated on the particles was estimated as if they were in solution (see Supporting Information, Table S 8). For instance, **SiμP–1** show 48.4 % cell viability when they are dosed at 22.1 nM of compound **1** , whereas **SiμP–3** show 49.6 % viability at 3.6 nM of **3**, and **SiμP–2** only show 5.9 % cell viability at 2.2 nM of **2**, evidencing an increased cytotoxicity when bipyridinium moieties are conjugated onto the microparticles.

The mechanism of toxicity of compound **1** in solution, which has been widely studied *in vitro*, using cell cultures, and *in vivo,*[50,51,60,61] involves the initial generation of superoxide anion, the formation of oxygen radicals, and the further lipid peroxidation, a radical chain reaction that spreads across polyunsaturated fatty acids (PUFA) of the cell membranes. The cytotoxicity mechanism is schematized and explained in the Supporting Information (Figure S 8). Although ROS are formed and lipid peroxidation occurs in healthy cells at basal levels, the extent of the oxidative state of cells determines their fate, where low levels of ROS and lipid peroxidation trigger the endogenous antioxidant systems (glutathione, vitamin E, superoxide dismutase, catalase, glutathione peroxidase) to counteract oxidation; but in contrast, high levels of lipid peroxidation trigger apoptosis or programmed necrosis.[60]

To observe if bipyridinium-functionalized microparticles follow a similar pathway, confocal fluorescence microscopy was used to image Hela cells upon being treated for different times with compound **1** in solution (100 μM, within the reported IC_{50} values) or with **SiμP-1** at lower doses (**SiμP**:cells 0.002:1 to 0.008:1). Cells were treated with CellROX® orange as a generalized fluorescent sensor to detect ROS in the cytoplasm, and were observed at λ_{ex} 561 nm and λ_{em} 566-759 nm (orange-red). In parallel, brightfield mode and blue emission (λ_{ex} 405 nm and λ_{em} 410-471 nm) were acquired to observe changes in cell morphology and composition. It has been reported that the spontaneous photon emission (SPE), occurring in lipid peroxidation, is attributed to excited states created during oxidative metabolic reactions. The main source of SPE is the slow spontaneous decomposition of lipid peroxides and endoperoxides, generating species such as singlet oxygen and excited triplet carbonyl groups. As well, the bimolecular reaction of alkoxy radicals lead to excited triplet carbonyl groups. Upon relaxation, excited carbonyl groups emit light in the blue region, whereas the bimolecular reaction of singlet oxygen emits light in the red region. Thus, imaging their luminescence could be used as a non-destructive technique capable of detecting lipid peroxidation in tissues. [61,62]

Figure 8 shows overlapped Z-projections of untreated cells, or cells treated with compound **1** for 1, 2, 4, or 24 h, or treated with **SiμP-1** for 2, 4, or 24 h. After either 1 or 2-h incubation with **1** in solution, the cells start to show signs of lipid peroxidation, being less transparent in the brightfield than untreated cells, which indicates either change in the composition or in the arrangement of the lipid bilayer, and showing higher number of vesicles of 400 – 900 nm in diameter. Higher blue emission was observed in these cells, especially coming from the vesicles, suggesting accumulation and reaction of alkoxy and peroxyl lipid radicals during lipid peroxidation. Incubation for longer times (4 or 24 h) shows increased sings of lipid peroxidation, including the blebbing of the cell membrane, indicating start of apoptosis, also observed in Figure 7.

In contrast, a higher extent of lipid peroxidation is associated to lower cytosolic ROS levels. After 2-h incubation cytosolic ROS concentrations remained similar to those of untreated cells (see Supporting Information Figure S 9), but decreased significantly after 4-h incubation. The ROS species induced by bipyridinium (initial superoxide and subsequent hydroxyl and peroxyl radicals) show very low stability. Whereas the estimated half-life of H_2O_2 is 10^{-3} s, and permits its diffusion to 1 μm from its origin,[63] the half-life of hydroxyl radical ($^{\bullet}OH$) is around 10^{-6} s,[64]

and that of superoxide ($O_2^{\bullet -}$) is only 10^{-9} s, indicating that they should immediately react with directly proximal substrates such as proteins and PUFA in the cell membrane.[63] The lipid radicals formed can in turn react with molecular oxygen and other ROS in the cytoplasm, leading to their eventual depletion.

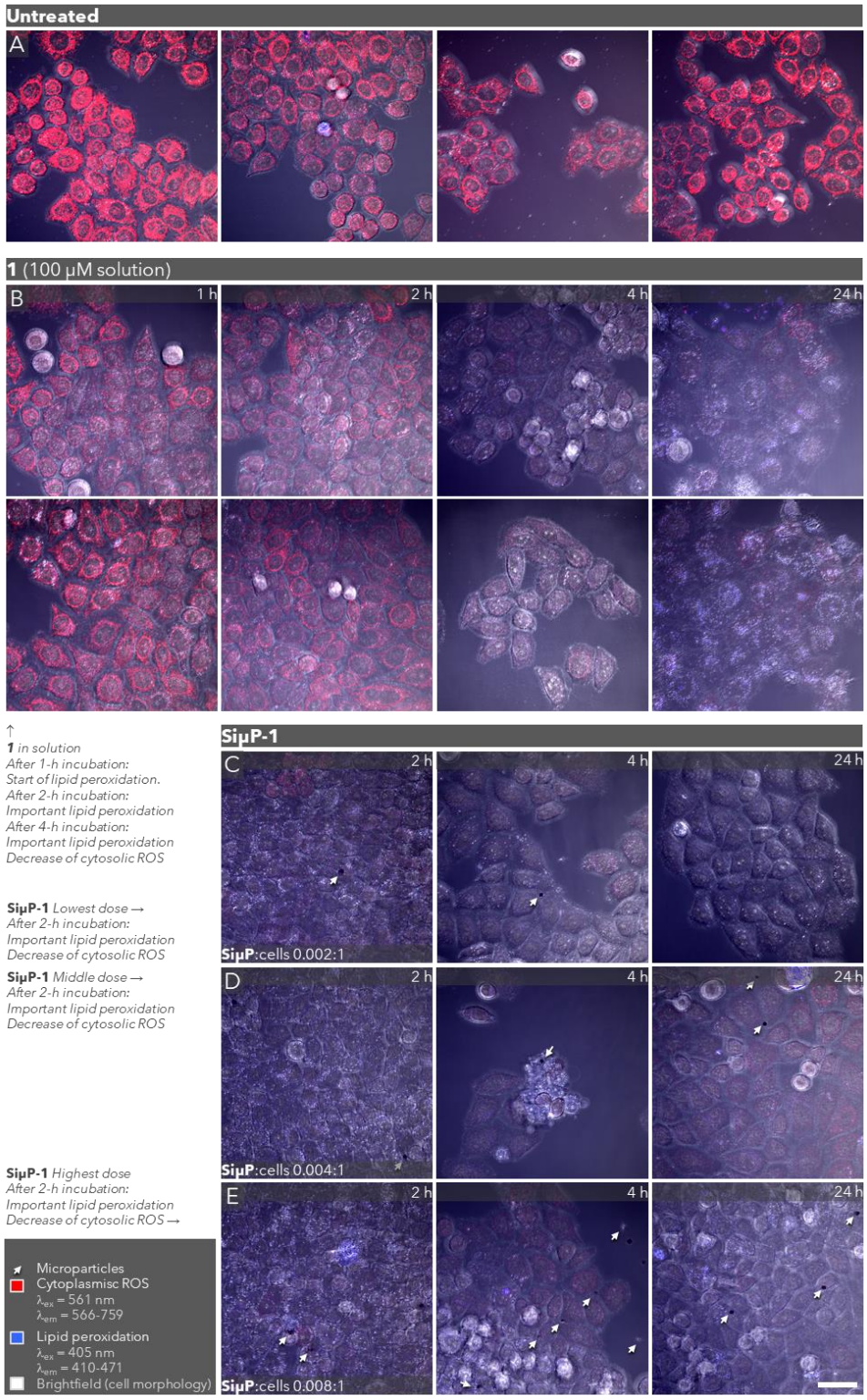

*Figure 8. Confocal fluorescence microscopy images (Z-projections) of (A) untreated Hela cells, or Hela cells treated with (B) 100 µM **1** in solution for 1, 2, 4, or 24 h, or treated with **SiµP-1** at (C) **SiµP**:cells 0.002: 1, (D) **SiµP**:cells 0.004: 1, (E) **SiµP**:cells 0.008: 1, for 2, 4, or 24 h. Upon 4-h incubation with **1**, important lipid peroxidation occurs leading to changes in cell morphology, with decreased transparency (brightfield), increased blue-emission, and decreased cytosolic ROS (red). Incubation with **SiµP-1** for 2 h leads to important lipid peroxidation, similar to that observed with 4-h incubation with **1** in solution. Scale bar represents 40 µm.*

Incubation with **SiμP-1** for 2 h, already at the lowest dose (**SiμP**:cells 0.002:1), led to significantly lower cytosolic ROS and important lipid peroxidation, similar to the 4-h incubation with **1** in solution. Lipid peroxidation starts in the cells internalizing particles, and spreads out across the proximal cells, as observed in **¡Error! No se encuentra el origen de la referencia.** D, 4 h. At the lowest dose, the equivalent concentration of bipyridinium units is 0.6 nM if they were in solution, evidencing a much higher efficiency when they are onto the microparticles. The close contact of the particles with the cell membrane due to strong multivalent interactions between the microparticles and the cell membrane, and due to sedimentation, might facilitate superoxide, hydroxyl, and peroxyl radicals to react with PUFA molecules, greatly increasing the speed of lipid peroxidation as compared to solution.

The membrane integrity loss induced by the microparticles was also confirmed by incubating Hela cells with the microparticles at low confluency (≈10 %) and higher **SiμP**:cells ratios, permitting an easier observation of their morphology and their interaction with the particles (see Supporting Information, Figure S 10). After 24-h incubation, the cells internalizing particles can completely lose their membrane integrity and release the microparticles, evidencing that each particle could be internalized in more than one cell during incubation. As observed by their morphology, apoptosis occurs not only in cells with particles internalized, but also on the neighboring cells, similar to observations at lower confluency (Figure 7 and Figure 8), in line with the radical chain reaction spreading across membranes.

These observations suggest that the mechanism of cytotoxicity of the bipyridinium-functionalized microparticles is similar to that of compound **1** in solution, but the microparticles can induce the cytotoxic effects in shorter times and to a much higher extent, with strong dependence on the number and type of particles administered.

Nonetheless, their high stability and self-renewing ability could possibly lead to further toxicity effects if they are left within the body. Even though it is true that polysilicon could be oxidized intracellularly to silicon oxide over time, and the latter can be biodegraded by dissolution of silicic acid into the aqueous medium,[65] the removal of the particles after exerting their toxicity could be considered. As their negligible self-diffusion helps the particles remain in place, they could be removed depending on the characteristics of the tumor tissue (surgical removal / suction techniques as in liposuction procedures). The administration of antioxidants such as α-tocopherol (vitamin E) could help stopping the radical chain reactions remaining in surrounding tissues, as they can react with lipid radicals becoming stable radicals.[35] Nonetheless, its high lipophilicity limits its distribution and diffusion across tissues, for which the administration of water-soluble analogs, or the use of liposomal preparations are needed to improve their efficacy.[51]

Conclusions

As a suitable system to improve the efficacy and selectivity towards cancerous cells, bipyridinium-derived compounds **1**, **2**, and **3** were selected for their ability to induce cytotoxicity in a range of potentials normally achieved in intracellular conditions and in a self-renewing fashion, and were covalently conjugated onto polysilicon microparticles (**SiμP**). The system was designed to increase the selectivity by means of three aspects: the size of microparticles eliminating their diffusion to surrounding tissues, the EPR effect maximizing their retention within the tumor, and the covalent immobilization of compounds onto the microparticles avoiding their release to solution and further diffusion.

Microparticles can be homogeneously functionalized with bipyridinium-containing compounds of different architectures, where the open chain structure of **1** permits a more densely packed SAM than the cyclic structures of **2** and **3**. They can be well internalized in cancerous Hela cells leading to several cytotoxic effects, including ROS-mediated lipid peroxidation, nuclear and cell membranes integrity loss, and overall decreased viability as observed

by intracellular and total esterase activity. Unfunctionalized particles are mainly non-cytotoxic, whereas bipyridinium-functionalized induce lipid peroxidation in their host cell and in the neighboring cells in less than 2 h. Functionalized particles importantly reduce cell viability at very low **SiμP**:cells ratios, leading to *cytotoxicity per particle* values of 6.4±0.7, 25.5±8.4, and 4.9±0.8 cell/**SiμP**, for **SiμP−1**, **SiμP−2,** and **SiμP−3**, respectively. Considering the number of moieties conjugated, the *cytotoxicity per bipy* values suggest that the less densely packed arrangement of bipyridinium units in cyclic structures (**SiμP−2** and **SiμP−3**) may account for a higher cytotoxic efficiency than in an open chain structure (**SiμP−1**). Nonetheless, the extended structure of bipyridinium (**SiμP−3**) may decrease their efficiency as compared to non-extended (**SiμP−2**), in line with the lower reduction potential in solution. The compounds conjugated display cytotoxicity at doses representing nanomolar concentrations if they were in solution, 3 orders of magnitude below IC_{50} values reported.

The highly efficient cytotoxicity of bipyridinium-functionalized microparticles might be promoted by their self-renewing ability, their possibility to internalize in more than one cell, and their proximity to the cell membrane due to strong multivalency interactions and sedimentation, facilitating the immediate reaction of the oxygen radicals with PUFA and increasing the speed of lipid peroxidation. The great extent of lipid peroxidation in short incubation times, and at low concentration of microparticles or bipyridinium units, is in line with the decreased cell viability induced, where the overall cytotoxic efficiency is reflected in the high *cytotoxicity per particle* and *cytotoxicity per bipy* values observed.

The fabrication of the **SiμP** based on silicon technologies allows a high reproducibility and control of the microparticles dimensions. The microparticles can be observed even under simple brightfield and fluorescence microscopies. They could be directly injected in suspension within the tumor, with control over the number of particles and the amount of compound administered, and could be further eliminated upon removal of the damaged tissue and treatment with antioxidants such as vitamin E. Looking to the future, the inclusion of magnetic materials during particle fabrication could improve their controlled elimination, while their possibility for hybrid functionalization could combine more functionalities in a single silicon chip, for example, the conjugation of antibodies on their surface may also provide increased active tumor targeting.[14,66]

Materials and Methods

Materials and solvents

MilliQ water (18 MΩ cm) was used in all the experiments. Dichloromethane 99.8 % (DCM), *N,N*-Dimethyl formamide (DMF), Isopropanol (IPA), Ethanol (EtOH), Sulfuric acid 98 % (H_2SO_4), Hydrogen peroxide solution 30 % (H_2O_2), Ammonium hydroxide solution 28 % (NH_4OH), Ethanol, Acetone (99.5 %), Acetonitrile anhydrous (99.8 %) (MeCN), (3-Aminopropyl)triethoxysilane (APTES), and 11-Bromoundecyltrichlorosilane 95 % (BUTCS) were purchased from abcr, Iodomethane 99 %, Propargyl chloride, Triethylamine (Et_3N), *N*-Hydroxysuccinimide (NHS), *N*-(3-Dimethylaminopropyl)-*N*′-ethylcarbodiimide hydrochloride (EDC), Tetrabutylammonium hexafluorophosphate (TBA·PF_6), Copper(I) bromide (CuBr), *N,N,N*′,*N*′′,*N*′′-Pentamethyldiethylenetriamine (PMDETA), (+)-Sodium L-ascorbate, tributylamine, 4,4′-Bipyridine, Parafilm® M, Phosphate-buffered saline (PBS) tablets, and Live/Dead Cell Double Staining Kit were purchased from Sigma. Hoechst 33342, Trihydrochloride, Trihydrate - 10 mg/mL Solution in Water and Gibco Dulbecco's Modified Eagle Medium (DMEM) were purchased from Thermo Fisher Scientific. Image-iT Fixative Solution (4 % formaldehyde, methanol-free) (PFA) was purchased from Invitrogen. ROS fluorescent probe 2',7'-Dichlorofluorescein diacetate was purchased from Cayman chemical.

Solutions

Piranha solution was prepared by mixing H_2SO_4 with H_2O_2 solution in a proportion of 7:3 (v:v). Basic solution was prepared by mixing NH_4OH solution with H_2O_2 solution and water in a proportion of 1:1:5 (v:v:v). PBS (10 mM phosphate) solution was prepared according to manufacturer's instructions.

Synthesis of bipyridinium compounds

Compound **1** was synthesized by dissolving 4,4'-bipyridine (0.5 g, 3.2 mmol) in dry MeCN (100 mL) under magnetic stirring. Methyl iodide (4.54 g, 32 mmol) was added and the solution was kept under reflux for 24 h. The orange-red solid precipitate was filtered under vacuum, washed thoroughly using MeCN and acetone. The precipitate was dissolved in water and a saturated aqueous solution of ammonium hexafluorophosphate was added. The precipitate was recovered by centrifugation, after which the supernatant was removed, and the solid was further washed by resuspension-centrifugation cycles using water (3 x 1 mL). The solid was dried overnight under vacuum to obtain compound **1**. Purity was confirmed by TLC and identity was confirmed by ^{1}H NMR. Compound **2** was synthesized by adapting a protocol for the synthesis of the azide-substituted *bluebox* ($CBPQT^{4+}$-N_3),[67] and compound **3** was synthesized by adapting a protocol for the synthesis of the *m*-ExBox.[68] The synthesis and molecular characterization of **2** and **3** will be published elsewhere.

Differential Pulse Voltammetry (DPV)

DMF was degassed in a sealed vial with a stream of nitrogen for 10 min and was used in all the DPV experiments. The working vial and the reference electrode were cleaned with DMF. 1 mg of compound (either **1**, **2**, or **3**) was dissolved in degassed DMF (1 mL) containing TBA·PF_6 and was placed in the working vial. Additional degassed DMF (2 mL) was added to reach enough volume to cover the electrodes. A working electrode, a Pt counter electrode, and a reference electrode (ground) were mounted in the working vial and the system was sealed with parafilm®. Nitrogen was bubbled through the solution for an additional 3 min. DPV analyses of the three different compounds in solution were acquired using Gamry Framework software, setting the analysis from 0.5 V to −2.5 V with a scan rate of 100 s^{-1} and a step size of 5 mV.

Cleaning and activation of silicon wafers

Stage 1: Wafers (0.25 cm^2) were first washed with water (2 x 5 mL) and ethanol (2 x 5 mL) and then dried with a stream of nitrogen. **Stage 2**: Subsequently, the wafers were activated by immersing them in piranha solution for one hour at room temperature under orbital shaking, after which the wafers were rinsed with water (2 x 5 mL) and dried with a stream of nitrogen. Wafers were then immersed in basic solution for 30 min at room temperature under orbital shaking, rinsed with water (2 x 5 mL), and dried with nitrogen.

*Functionalization of silicon wafers with **1** (**Si—1**)*

Stage 3: Previously activated wafers (Stages 1 and 2) were immersed in a 5 % solution of BUTCS solution in DCM and were left under orbital shaking overnight at room temperature, after which they were rinsed with DCM (2 x5 mL) and dried with a stream of nitrogen. **Stage 4**: Wafers were immersed in a 43 mM solution of 4,4'-bipyridine in IPA and were left under orbital shaking overnight at room temperature, after which they were rinsed with IPA (2 x5 mL) and dried with nitrogen. **Stage 5**: Finally, wafers were immersed in a 200 mM solution of iodomethane in DCM and were left under orbital shaking for 48 h at room temperature. Wafers were rinsed with DCM (2 x 5 mL) and dried with nitrogen.

*Functionalization of silicon wafers with **2** (**Si—2**)*

Stage 3: Previously activated wafers (Stages 1 and 2) were immersed in a solution of APTES in ethanol (1:19) and were left at room temperature under orbital shaking for 3 h, after which wafers were washed with ethanol (2 x 5 mL) and acetone (2 x 5 mL) and dried with a stream of nitrogen. **Stage 4**: Wafers were immersed in a solution containing 120 mM propargyl chloride, 60 mM tributylamine, and 60 mM triethylamine in DCM and kept at room

temperature under orbital shaking for 7 h. Afterwards, wafers were rinsed with acetone (2 x 5 mL) and dried with a stream of nitrogen. **Stage 5**: Wafers were immersed in a solution containing 10 mM **2**, 0.1 mM CuBr, 0.1 mM PMDETA, and 5 mM sodium ascorbate in DMF:H_2O (98:2), and the flask containing the wafers was sealed, bubbled with nitrogen for 5 min, and kept overnight at room temperature with magnetic stirring. Afterwards, wafers were washed with DMF (2 x 5 mL) and acetone (2 x 5 mL) and dried with nitrogen.

*Functionalization of silicon wafers with **3** (**Si—3**)*

Stage 5: Wafers previously activated (Stages 1 and 2) and functionalized with APTES (Stage 3) were immersed in a solution containing 0.22 mM **3**, 4.9 mM NHS, 4 mM EDC, and 0.02 % of Et_3N in MeCN and then kept under magnetic stirring for 4 h at room temperature. Wafers were then washed with MeCN (2 x 5 mL) and acetone (2 x 5 mL) and dried with nitrogen.

Contact angle measurements

Contact angle measurements were performed in air using a Thetalite100 goniometer equipped with the software OneAttension (Finland). A 3 µL drop of milliQ water was applied on the surface and the mean of 10 contact angle measurements was obtained. At least three replicates for each sample were analyzed.

X-Ray Photoelectron Spectroscopy (XPS)

Silicon oxide wafers with the polysilicon microparticles on top were analyzed using a Thermo ESCAlab 250 Xi X-Ray Photoelectron Spectroscopy (XPS) instrument controlled by ThermoFisher Avantage v5 software. A survey was performed from each surface after each functionalization stage, and further analysis of the atomic content of Br3d, Si2p, C1s, N1s, O1s, and I3d was performed. The atomic content of each element relative to Si2p was obtained.

*Confocal fluorescence microscopy of **Si—3** wafers*

Si—3 wafers were observed in a Leica SP8 Confocal Fluorescence Microscope in the Biological Imaging Facility (RRID:SCR_017767) at Northwestern University, controlled by FluorEscence V.35 software. A laser set at λex = 405 nm (10 % intensity) and a HyD2 detector set at λem = 420 ± 11 nm and smart gain 390 % were used to observe fluorescence from **3**. The detection of the silicon surface was achieved in reflectance mode. Pinhole was set at 1 and 8.5X zoom was used.

*Functionalization of Silicon microparticles (**SiµP**) with bipyridinium compounds*

Cleaning of unfunctionalized microparticles (SiµP). **Stage 1:** As a control for different experiments, unfunctionalized microparticles (**SiµP**) (ca. 1.5 million per Eppendorf) initially suspended in ethanol (1 mL) were sedimented with centrifugation and supernatant was removed. Particles were washed with water (2 x 100 µL) using centrifugation-resuspension cycles (10 min, 13400 rpm) and finally resuspended in 150 µL PBS.

Activation of microparticles. Stage 2: SiµP (ca. 1.5 million per Eppendorf) initially suspended in ethanol (1 mL) were sedimented with centrifugation and supernatant was removed. Particles were then activated by acid and basic treatment without prior cleaning in order to decrease particle loss. Briefly, piranha solution (100 µL) was added, microparticles were resuspended using sonication (10 s) and left under vortex at room temperature for 1 h. Microparticles were washed with isopropanol (2 x 900 µL) by centrifugation-resuspension cycles (10 min, 13400 rpm) and the supernatant was completely removed. Basic solution (100 µL) was then added to each Eppendorf tube, microparticles were resuspended using sonication and left under vortex at room temperature for 30 min. DMF (900 µL) was added, particles were sonicated and then centrifuged (10 min, 13400 rpm), and supernatant was removed.

Functionalization of SiμP–1. Stage 3: A 1.71 mM solution of BUTCS in DCM (300 μL) was added to previously activated microparticles (stage 2). The suspension was sonicated for 5 min and was left under vortex stirring overnight at room temperature. Afterwards, particles were washed with centrifugation-resuspension cycles (10 min, 13400 rpm) using DCM (1 x 800 μL) and IPA (1 x 800 μL), and supernatant was finally removed. **Stage 4:** A 83 mM solution of 4,4′-bipyridine in IPA (500 μL) was added to the microparticles. The reaction was carried out at room temperature for 3 h under sonication, after which IPA (500 μL) was added and particles were sedimented using centrifugation and supernatant was removed. **Stage 5:** A 800 mM solution of iodomethane in IPA (500 μL) was added to each tube. Microparticles were resuspended with sonication (1 min) and left under vortex for 48 h at room temperature. Particles were washed with centrifugation-resuspension cycles using IPA (2 x 1000 μL), and were resuspended in acetone (1000 μL) and stored at room temperature. Before further experiments, particles were centrifuged, the supernatant was removed, and the remaining solvent was completely evaporated using a stream of nitrogen (≈5 min) before being resuspended in the desired medium.

Functionalization of SiμP–2. **Stage 3:** A solution (200 μL) of APTES in ethanol (1:19) was added to previously activated **SiμP** (stage 2). The suspension was sonicated for 3 h at room temperature, after which particles were centrifuged and the supernatant was removed. **Stage 4:** A solution containing 558 mM propargyl chloride and 788 mM Et_3N in ethanol (260 μL) was added to the particles, and they were resuspended using sonication (30 s). The reaction was carried out under vortex stirring overnight at room temperature, after which particles were washed with centrifugation-resuspension cycles with ethanol (2 x 200 μL) using sonication, and the supernatant was finally removed. **Stage 5:** A solution containing 0.87 mM **2**, 0.087 mM $CuSO_4$, and 0.87 mM sodium ascorbate in DMF:H_2O (98:2) (200 μL) was added to the particles and they were resuspended using sonication (30 s). The reaction was left overnight under vortex stirring at room temperature. Particles were then washed with centrifugation-resuspension cycles using DMF:H_2O (98:2) (1 x 200 μL) and then acetone (1 x 200 μL). Particles were finally resuspended in acetone (1000 μL) and stored at room temperature. Before further experiments, particles were centrifuged, the supernatant was removed, and the remaining solvent was completely evaporated using a stream of nitrogen (≈5 min) before being resuspended in the desired medium.

Functionalization of SiμP–3. **Stage 5:** To the microparticles previously functionalized with APTES (stage 3), a solution containing 0.12 mM **3**, 2.65 mM NHS, and 2.08 mM EDC in DMF:H_2O:MeCN (56:31:13) (200 μL) was added. The particles were resuspended using sonication (30 s), and the reaction was kept overnight under vortex stirring at room temperature. Afterwards, particles were sonicated and were washed with centrifugation-resuspension cycles using DMF:H_2O:MeCN (56:31:13) (1 x 200 μL) and acetone (1 x 200 μL). Particles were finally resuspended in acetone (1000 μL) and stored at room temperature. Prior to conducting further experiments, particles were centrifuged, the supernatant was removed, and the remaining solvent was completely evaporated using a stream of nitrogen (≈5 min) before being resuspended in the desired medium.

Particle count

100 μL PBS (1x) were added to each well in transparent 96-well plates. Previously washed unfunctionalized (**SiμP**) and functionalized (**SiμP–1**, **SiμP–2**, **SiμP–3**) microparticles were resuspended in PBS (150 μL) using sonication, and 20 μL or 40 μL aliquots of each suspension were added to the different wells. Particles were counted using a Lionheart FX automated microscope. ImageJ particle-count plugin was used for counting the particles in the images. As the total sample volume in each well is known, as well as the dimensions of the region imaged, the volume of sample observed can be calculated (see Supporting Information, Table S5). Therefore, the total number of particles recovered after functionalization was estimated (see Supporting Information, Table S6).

*Internalization of unfunctionalized microparticles (**SiμP**) in Hela cells*

The internalization of unfunctionalized **SiμP** in cancerous Hela cells was studied using brightfield and confocal fluorescence microscopies. Cells grown to 80 % confluency (ca. 100,000 cells per well) were treated with different

volumes (10, 20, 40, and 80 µL) of a suspension of microparticles (≈417 **SiµP**/µL) in PBS. PBS was added to a final volume of 80 µL and DMEM (100 µL) was finally added. Cells were incubated for 24 h at 37°C and 5 % CO_2 and were later washed multiple times with PBS to remove non-internalized particles and detached cells. Samples were observed under brightfield microscopy using a Lionheart FX automated microscope. Images were taken on a LionheartFX (BioTek) microscope with an Olympus 10X PL FL Phase objective, yielding an image with pixel size dx = dy = 0.658 µm.

Internalization of the **SiµP** in cells was assessed by confocal fluorescence microscopy. Cells were treated with 20 or 40 µL of a suspension of microparticles (≈417 **SiµP**/µL) in PBS (**SiµP:**cells ratios 0.08:1 or 0.17:1, respectively), and DMEM to complete a final volume of 200 µL. After 24-h incubation with the microparticles, cells were fixed with 4 % PFA and stained with Alexa Fluor® 488 Phalloidin (targets filamentous actin) and Hoechst 33342 (targets DNA). Images were taken at 63x magnification (Leica HCX PL APO 63x/1.4NA) on a Leica SP8 confocal microscope, yielding an image with pixel size of dx = dy = 0.072 µm. DNA was detected at λ ex = 405 nm and λem = 480-500 nm. Actin was detected at λex = 488 nm and λem = 520-600 nm. **SiµP** were detected in reflectance mode at λ = 650 nm.

Cytotoxicity of functionalized microparticles in Hela cells

Hela cells were grown to ≈80 % confluency (approx. 100,000 cells per well). Unfunctionalized (**SiµP**) and functionalized (**SiµP−1**, **SiµP−2**, **SiµP−3**) particles were resuspended in 150 µL PBS (1x) using sonication. Cells were treated with 20 or 40 µL of the suspensions of microparticles in PBS. Untreated cells (20 or 40 µL in PBS) were processed in parallel as a control. DMEM was then added to obtain a final volume of 200 µL. Cells were incubated (37 °C, 5 % CO_2) for 24 h, were fixed with 4 % PFA, and stained with Live/Dead Cell Double Staining kit 30 min before being imaged. Cells were washed with PBS to remove fluorophores in solution, non-internalized particles, and detached dells, and were imaged using confocal fluorescence microscopy at λ ex = 488 nm and λ em = 520-560 nm (green), or λ ex = 600 nm and λ em = 635-700 nm (red). In parallel, samples were observed in brightfield mode to detect cell membranes and microparticles, while reflectance-mode data was acquired in some samples for easier visualization of the microparticles, yielding an image with pixel size of dx = dy = 0.072 µm. Non-fluorescent Calcein-AM (acetoxymethyl ester of calcein) is highly lipophilic and cell membrane permeable. Intracellular esterases then generate calcein in a viable cell emitting a strong green fluorescence (λ_{ex} 490 nm, λ_{em} 515 nm).

The *cell viability* [%] was calculated using ImageJ by quantifying the fluorescence in the green channel. For that, two different approaches were followed. In the first approach, the *cell viability* [%] was estimated as shown in the equation:

Eq. 1

$$Cell\ viability_{\ total\ esterase\ activity}[\%] = \frac{FI_{image}(sample)}{FI_{image}(untreated)} \cdot 100$$

Where FI_{image} is the integrated fluorescence intensity of the images. According to this approach, values reflect the total esterase activity of the sample after treatment with particles, and is influenced by the number and size of cells (cell confluency) remaining in the sample, as well as by the esterase activity of each cell. Thus, this approach is equivalent to other conventional methods for assessing the cell viability in solution such as MTT.[59]

In the second approach, areas of the image containing cells (n≥10) were delimited, and the mean fluorescence was quantified in such areas. Then, the *cell viability* [%] was then obtained as follows:

Eq. 2

$$Cell\ viability_{mean\ intracellular\ esterase\ activity}\ [\%] = \frac{MFI_{cells}(sample)}{MFI_{cells}\ (untreated)} \cdot 100$$

Where MFI_{cells} is the mean fluorescence intensity of cells. According to this approach, values are not influenced by the number and size of cells remaining in the sample, but they specifically reflect the esterase activity within cells after treatment with particles. The comparison of *cell viability* values using both approaches could provide information about the number and size of cells after treatment.

Using both approaches (eq. 1 and 2), the *cytotoxicity per particle* [cell/**SiμP**] was calculated according to the equation:

Eq. 3

$$Cytotoxicity\ per\ particle\ \left[\frac{cell}{\boldsymbol{Si}\mu\boldsymbol{P}}\right] = \left(\frac{100 - Cell\ viability}{100}\right)\left(\frac{n_{cells}}{n_{\mathbf{Si\mu P}}}\right)$$

Where n_{cells} is the estimated number of cells in each well at the start of the experiment (*ca.* 100 000), and $n_{\boldsymbol{Si\mu P}}$ is the total number of microparticles dosed to the cells. This proportion of cells to microparticles is also the inverse value of the **SiμP**:cells ratio [**SiμP**/cell].

Finally, the *cytotoxicity per bipy* [cell/bipy] was calculated as follows:

Eq. 4

$$Cytotoxicity\ per\ bipy\ [\frac{cell}{bipy}]\ = \frac{Cytotoxicity\ per\ particle}{bipy\ per\ particle}$$

Where *bipy per particle* [bipy/**SiμP**] is the total number of bipyridinium moieties conjugated per particle, considering the number of molecules conjugated and the number of bipyridinium moieties contained in each molecule.

To observe the mechanism of cytotoxicity of the microparticles, Hela cells were incubated in DMEM at ≈80% confluency (≈476000 cells per well), and were treated with compound **1** solution at a final concentration of 100 μM for 1, 2, 4, or 24 h, or with 10, 20, or 40 μL of a suspension of 97.6 **SiμP**/μL of **SiμP-1** (**SiμP**:cells 0.002:1, 0.004:1, or 0.008:1) for 2, 4, or 24 h. 30 min prior observation, cells were washed and incubated with CellROX® orange, after which they were washed and observed using a Zeiss LSM 880 confocal fluorescence microscope. Samples were observet at λ_{ex} 561 nm and λ_{em} 566-759 nm (orange-red), λ_{ex} 405 nm and λ_{em} 410-471 nm (violet-blue), and brightfield. Z-projections of the stacks acquired were made using ImageJ yielding an image with pixel size dx = dy = 0.208 μm.

To observe more easily the membrane integrity loss, Hela cells were grown to ≈10 % confluency in 96-well plates (ca. 12,500 cells per well). PBS (40 μL) and DMEM (100 μL) was added, and a suspension of microparticles (40 μL) in PBS was finally added. Cells were incubated for 24 h at 37°C and 5 % CO_2 for observing cells and their interaction with the microparticles. Samples were observed on a LionheartFX (BioTek) automated microscope with an Olympus 10X PL FL Phase objective. Images were acquired in brightfield mode yielding an image with pixel size dx = dy = 0.658 μm.

Acknowledgements

ERDF (FEDER) funds and Spanish government grants TEC2017-85059-C3-1 and 2-R, and PID2020-115663GB-C3-1 and 2 are acknowledged. D. Limón thanks Consortium for Advanced Studies Abroad (CASA) for a postdoctoral fellowship. J. F. Stoddart, K. Cai and Y. Beldjoudi thank Northwestern University for continuing support. Authors thank Manel Bosch from Scientific and Technological Centers of the University of Barcelona (CCITUB) for his kind support with cell cultures and microscopy experiments.

Supporting Information Available

Contact angle measurements of functionalized silicon wafers, XPS studies, functionalization of **SiμP** with bipyridinium compounds, confocal fluorescence microscopy images of **Si–3** wafers and of **SiμP–3** microparticles, particle count experiments, internalization in Hela cells, cytotoxicity quantification of functionalized microparticles in Hela cells, and cytotoxic effects at low confluency.

Financial Interests

Authors declare no financial interests.

References

(1) Fornari, F. A.; Randolph, J. K.; Yalowich, J. C.; Ritke, M. K.; Gewirtz, D. A. Interference by Doxorubicin with DNA Unwinding in MCF-7 Breast Tumor Cells. *Mol. Pharmacol.* **1994**, *45* (4), 694–656.

(2) Rajagopalan, P. T. R.; Zhang, Z.; McCourt, L.; Dwyer, M.; Benkovic, S. J.; Hammes, G. G. Interaction of Dihydrofolate Reductase with Methotrexate: Ensemble and Single-Molecule Kinetics. *Proc. Natl. Acad. Sci. U. S. A.* **2002**, *99* (21), 13481–13486.

(3) Kollmannsberger, C.; Mross, K.; Jakob, A.; Kanz, L.; Bokemeyer, C. Topotecan – A Novel Topoisomerase I Inhibitor: Pharmacology and Clinical Experience. *Oncology* **1999**, *56* (1), 1–12.

(4) Roskoski, R. A Historical Overview of Protein Kinases and Their Targeted Small Molecule Inhibitors. *Pharmacol. Res.* **2015**, *100*, 1–23.

(5) Jordan, M. A.; Wilson, L. Microtubules As a Target for Anticancer Drugs. *Nat. Rev. Cancer* **2004**, *4* (April), 253–265.

(6) Oun, R.; Moussa, Y. E.; Wheate, N. J. The Side Effects of Platinum-Based Chemotherapy Drugs: A Review for Chemists. *Dalt. Trans.* **2018**, *47* (19), 6645–6653.

(7) Frank, M.; Hennenberg, E. M.; Eyking, A.; Rünzi, M.; Gerken, G.; Scott, P.; Parkhill, J.; Walker, A. W.; Cario, E. TLR Signaling Modulates Side Effects of Anticancer Therapy in the Small Intestine. *J. Immunol.* **2015**, *194* (4), 1983–1995.

(8) Russo, S.; Cinausero, M.; Gerratana, L.; Bozza, C.; Iacono, D.; Driol, P.; Deroma, L.; Sottile, R.; Fasola, G.; Puglisi, F. Factors Affecting Patient's Perception of Anticancer Treatments Side-Effects: An Observational Study. *Expert Opin. Drug Saf.* **2014**, *13* (2), 139–150.

(9) Accordino, M. K.; Neugut, A. I.; Hershman, D. L. Cardiac Effects of Anticancer Therapy in the Elderly. *J. Clin. Oncol.* **2014**, *32* (24), 2654–2661.

(10) Hohenforst-Schmidt, W.; Zarogoulidis, P.; Darwiche, K.; Vogl, T.; Goldberg, E. P.; Huang, H.; Simoff, M.; Li, Q.; Browning, R.; Turner, F. J.; et al. Intratumoral Chemotherapy for Lung Cancer: Re-Challenge Current Targeted Therapies. *Drug Des. Devel. Ther.* **2013**, *7*, 571–583.

(11) Fang, J.; Nakamura, H.; Maeda, H. The EPR Effect: Unique Features of Tumor Blood Vessels for Drug Delivery, Factors Involved, and Limitations and Augmentation of the Effect. *Adv. Drug Deliv. Rev.* **2011**, *63* (3), 136–151.

(12) Iyer, A. K.; Khaled, G.; Fang, J.; Maeda, H. Exploiting the Enhanced Permeability and Retention Effect for Tumor Targeting. *Drug Discov. Today* **2006**, *11* (17–18), 812–818.

(13) Ding, Y.; Xu, Y.; Yang, W.; Niu, P.; Li, X.; Chen, Y.; Li, Z.; Liu, Y.; An, Y.; Liu, Y.; et al. Investigating the EPR Effect of Nanomedicines in Human Renal Tumors via Ex Vivo Perfusion Strategy. *Nano Today* **2020**, *35*, 100970.

(14) Yan, L.; Shen, J.; Wang, J.; Yang, X.; Dong, S.; Lu, S. Nanoparticle-Based Drug Delivery System: A Patient-Friendly Chemotherapy for Oncology. *Dose-Response* **2020**, *18* (3), 1–12.

(15) Valente, K. P.; Suleman, A.; Brolo, A. G. Exploring Diffusion and Cellular Uptake: Charged Gold Nanoparticles in an in Vitro Breast Cancer Model. *ACS Appl. Bio Mater.* **2020**, *3* (10), 6992–7002.

(16) Dai, Q.; Wilhelm, S.; Ding, D.; Syed, A. M.; Sindhwani, S.; Zhang, Y.; Chen, Y. Y.; Macmillan, P.; Chan, W.

C. W. Quantifying the Ligand-Coated Nanoparticle Delivery to Cancer Cells in Solid Tumors. *ACS Nano* **2018**, *12* (8), 8423–8435.

(17) Park, K. Questions on the Role of the EPR Effect in Tumor Targeting. *J. Control. Release* **2013**, *172* (1), 391.

(18) Cruickshank Miller, C. The Stokes-Einstein Law for Diffusion in Solution. *Proc. R. Soc. A. Math. Phys. Eng. Sci.* **1924**, *106* (740), 724–749.

(19) Peulen, T. O.; Wilkinson, K. J. Diffusion of Nanoparticles in a Biofilm. *Environ. Sci. Technol.* **2011**, *45* (8), 3367–3373.

(20) Shi, W.; Wang, J.; Fan, X.; Gao, H. Size and Shape Effects on Diffusion and Absorption of Colloidal Particles near a Partially Absorbing Sphere: Implications for Uptake of Nanoparticles in Animal Cells. *Phys. Rev. E - Stat. Nonlinear, Soft Matter Phys.* **2008**, *78* (6), 1–11.

(21) Habimana, O.; Steenkeste, K.; Fontaine-Aupart, M. P.; Bellon-Fontaine, M. N.; Kulakauskas, S.; Briandet, R. Diffusion of Nanoparticles in Biofilms Is Altered by Bacterial Cell Wall Hydrophobicity. *Appl. Environ. Microbiol.* **2011**, *77* (1), 367–368.

(22) Kim, B.; Han, G.; Toley, B. J.; Kim, C. K.; Rotello, V. M.; Forbes, N. S. Tuning Payload Delivery in Tumour Cylindroids Using Gold Nanoparticles. *Nat. Nanotechnol.* **2010**, *5* (6), 465–472.

(23) Cho, E. C.; Zhang, Q.; Xia, Y. The Effect of Sedimentation and Diffusion on Cellular Uptake of Gold Nanoparticles. *Nat. Nanotechnol.* **2011**, *6* (6), 385–391.

(24) Safwat, M. A.; Soliman, G. M.; Sayed, D.; Attia, M. A. Fluorouracil-Loaded Gold Nanoparticles for the Treatment of Skin Cancer: Development, in Vitro Characterization, and in Vivo Evaluation in a Mouse Skin Cancer Xenograft Model. *Mol. Pharm.* **2018**, *15* (6), 2194–2205.

(25) Sonavane, G.; Tomoda, K.; Sano, A.; Ohshima, H.; Terada, H.; Makino, K. In Vitro Permeation of Gold Nanoparticles through Rat Skin and Rat Intestine: Effect of Particle Size. *Colloids Surfaces B Biointerfaces* **2008**, *65* (1), 1–10.

(26) Larese Filon, F.; Crosera, M.; Adami, G.; Bovenzi, M.; Rossi, F.; Maina, G. Human Skin Penetration of Gold Nanoparticles through Intact and Damaged Skin. *Nanotoxicology* **2011**, *5* (4), 493–501.

(27) Gupta, R.; Rai, B. Effect of Size and Surface Charge of Gold Nanoparticles on Their Skin Permeability: A Molecular Dynamics Study. *Sci. Rep.* **2017**, *7* (October 2016), 1–13.

(28) Lerche, D. Comprehensive Characterization of Nano-and Microparticles by in-Situ Visualization of Particle Movement Using Advanced Sedimentation Techniques. *KONA Powder Part. J.* **2019**, *36* (36), 156–186.

(29) Serda, R. E.; Gu, J.; Bhavane, R. C.; Liu, X. W.; Chiappini, C.; Decuzzi, P.; Ferrari, M. The Association of Silicon Microparticles with Endothelial Cells in Drug Delivery to the Vasculature. *Biomaterials* **2009**, *30* (13), 2440–2448.

(30) Salonen, J.; Laitinen, L.; Kaukonen, A. M.; Tuura, J.; Björkqvist, M.; Heikkilä, T.; Vähä-Heikkilä, K.; Hirvonen, J.; Lehto, V. P. Mesoporous Silicon Microparticles for Oral Drug Delivery: Loading and Release of Five Model Drugs. *J. Control. Release* **2005**, *108* (2–3), 362–374.

(31) Haidary, S. M.; Córcoles, E. P.; Ali, N. K. Nanoporous Silicon as Drug Delivery Systems for Cancer Therapies. *J. Nanomater.* **2012**, *2012*.

(32) Anglin, E. J.; Cheng, L.; Freeman, W. R.; Sailor, M. J. Porous Silicon in Drug Delivery Devices and Materials. *Adv. Drug Deliv. Rev.* **2008**, *60* (11), 1266–1277.

(33) Agusil, J. P.; Torras, N.; Duch, M.; Esteve, J.; Pérez-García, L.; Samitier, J.; Plaza, J. A. Highly Anisotropic Suspended Planar-Array Chips with Multidimensional Sub-Micrometric Biomolecular Patterns. *Adv. Funct. Mater.* **2017**, *27* (13).

(34) Torras, N.; Agusil, J. P.; Vázquez, P.; Duch, M.; Hernández-Pinto, A. M.; Samitier, J.; De La Rosa, E. J.; Esteve, J.; Suárez, T.; Pérez-García, L.; et al. Suspended Planar-Array Chips for Molecular Multiplexing at the Microscale. *Adv. Mater.* **2016**, *28* (7), 1449–1454.

(35) Novo, S.; Penon, O.; Barrios, L.; Nogués, C.; Santaló, J.; Durán, S.; Gómez-Matínez, R.; Samitier, J.; Plaza, J. A.; Pérez-García, L.; et al. Direct Embryo Tagging and Identification System by Attachment of Biofunctionalized Polysilicon Barcodes to the Zona Pellucida of Mouse Embryos. *Hum. Reprod.* **2013**, *28* (6), 1519–1527.

(36) Penon, O.; Novo, S.; Druán, S.; Ibañez, E.; Nogués, C.; Samitier, J.; Duch, M.; Plaza, J. A.; Pérez-García, L. Efficient Biofunctionalization of Polysilicon Barcodes for Adhesion to the Zona Pellucida of Mouse Embryos. *Bioconjug. Chem.* **2012**, No. 23, 2392–2402.

(37) Fernández-Rosas, E.; Gómez, R.; Ibañez, E.; Barrios, L.; Duch, M.; Esteve, J.; Plaza, J. A.; Nogués, C. Internalization and Cytotoxicity Analysis of Silicon-Based Microparticles in Macrophages and Embryos. *Biomed. Microdevices* **2010**, *12* (3), 371–379.

(38) Alea-Reyes, M. E.; Rodrigues, M.; Serrà, A.; Mora, M.; Sagristá, M. L.; González, A.; Durán, S.; Duch, M.; Plaza, J. A.; Vallés, E.; et al. Nanostructured Materials for Photodynamic Therapy: Synthesis, Characterization and in Vitro Activity. *RSC Adv.* **2017**, *7* (28), 16963–16976.

(39) Durán, S.; Duch, M.; Patiño, T.; Torres, A.; Penon, O.; Gómez-Martínez, R.; Barrios, L.; Esteve, J.; Nogués, C.; Pérez-García, L.; et al. Technological Development of Intracellular Polysilicon-Chromium-Gold Chips for Orthogonal Chemical Functionalization. *Sensors Actuators, B Chem.* **2015**, *209*, 212–224.

(40) Fernández-Rosas, E.; Baldi, A.; Ibañez, E.; Barrios, L.; Novo, S.; Esteve, J.; Plaza, J. A.; Duch, M.; Gómez, R.; Castell, O.; et al. Chemical Functionalization of Polysilicon Microparticles for Single-Cell Studies. *Langmuir* **2011**, *27* (13), 8302–8308.

(41) Gómez-Martínez, R.; Vázquez, P.; Duch, M.; Muriano, A.; Pinacho, D.; Sanvicens, N.; Sánchez-Baeza, F.; Boya, P.; De La Rosa, E. J.; Esteve, J.; et al. Intracellular Silicon Chips in Living Cells. *Small* **2010**, *6* (4), 499–502.

(42) Bruce, G.; Samperi, M.; Amabilino, D. B.; Duch, M.; Plaza, J. A.; Pérez-García, L. Singlet Oxygen Generation from Porphyrin-Functionalized Hexahedral Polysilicon Microparticles. *J. Porphyr. Phthalocyanines* **2019**, *23* (1–2), 223–233.

(43) Ashton, P. R.; Balzani, V.; Becher, J.; Credi, A.; Fyfe, M. C. T.; Mattersteig, G.; Menzer, S.; Nielsen, M. B.; Raymo, F. M.; Stoddart, J. F.; et al. A Three-Pole Supramolecular Switch. *J. Am. Chem. Soc.* **1999**, *121* (16), 3951–3957.

(44) Cai, K.; Cui, B.; Song, B.; Wang, H.; Qiu, Y.; Jones, L. O.; Liu, W.; Shi, Y.; Vemuri, S.; Shen, D.; et al. Radical Cyclic [3]Daisy Chains. *Chem* **2021**, *7* (1), 174–189.

(45) Liu, Y.; Flood, A. H.; Bonvallet, P. A.; Vignon, S. A.; Northrop, B. H.; Tseng, H. R.; Jeppesen, J. O.; Huang, T. J.; Brough, B.; Baller, M.; et al. Linear Artificial Molecular Muscles. *J. Am. Chem. Soc.* **2005**, *127* (27), 9745–9759.

(46) Roy, I.; Goswami, S.; Young, R. M.; Schlesinger, I.; Mian, M. R.; Enciso, A. E.; Zhang, X.; Hornick, J. E.; Farha, O. K.; Wasielewski, M. R.; et al. Photon Upconversion in a Glowing Metal-Organic Framework. *J.*

Am. Chem. Soc. **2021**, *143* (13), 5053–5059.

(47) Roy, I.; Bobbala, S.; Zhou, J.; Nguyen, M. T.; Nalluri, S. K. M.; Wu, Y.; Ferris, D. P.; Scott, E. A.; Wasielewski, M. R.; Stoddart, J. F. ExTzBox: A Glowing Cyclophane for Live-Cell Imaging. *J. Am. Chem. Soc.* **2018**, *140* (23), 7206–7212.

(48) Garci, A.; Beldjoudi, Y.; Kodaimati, M. S.; Hornick, J. E.; Nguyen, M. T.; Cetin, M. M.; Stern, C. L.; Roy, I.; Weiss, E. A.; Stoddart, J. F. Mechanical-Bond-Induced Exciplex Fluorescence in an Anthracene-Based Homo[2]Catenane. *J. Am. Chem. Soc.* **2020**, *142* (17), 7956–7967.

(49) Baer, K. N. Paraquat. *Encyclopedia of Toxicology (Second Edition)*; Elsevier, 2005; pp 329–330.

(50) Bus, J. S.; Aust, S. D.; Gibson, J. E. Paraquat Toxicity: Proposed Mechanism of Action Involving Lipid Peroxidation. *Environ. Health Perspect.* **1976**, *16*, 139–146.

(51) Suntres, Z. E. Role of Antioxidants in Paraquat Toxicity. *Toxicology* **2002**, *180* (1), 65–77.

(52) Wang, S.; Wu, H.; Chen, F.; Zhang, Y.; Zhang, Y.; Sun, B. The Antitumor Activity of 4,4′-Bipyridinium Amphiphiles. *RSC Adv.* **2019**, *9* (57), 33023–33028.

(53) Sheeney-Haj-Ichia, L.; Wasserman, J.; Willner, I. CdS-Nanoparticle Architectures on Electrodes for Enhanced Photocurrent Generation. *Adv. Mater.* **2002**, *14* (18), 1323–1326.

(54) Liang, W.; Yi, W.; Li, S.; Yuan, R.; Chen, A.; Chen, S.; Xiang, G.; Hu, C. A Novel, Label-Free Immunosensor for the Detection of α-Fetoprotein Using Functionalised Gold Nanoparticles. *Clin. Biochem.* **2009**, *42* (15), 1524–1530.

(55) Cheng, C. A.; Deng, T.; Lin, F. C.; Cai, Y.; Zink, J. I. Supramolecular Nanomachines as Stimuli-Responsive Gatekeepers on Mesoporous Silica Nanoparticles for Antibiotic and Cancer Drug Delivery. *Theranostics* **2019**, *9* (11), 3341–3364.

(56) Wen, J.; Yang, K.; Liu, F.; Li, H.; Xu, Y.; Sun, S. Diverse Gatekeepers for Mesoporous Silica Nanoparticle Based Drug Delivery Systems. *Chem. Soc. Rev.* **2017**, *46* (19), 6024–6045.

(57) Flood, A. H.; Nygaard, S.; Laursen, B. W.; Jeppesen, J. O.; Stoddart, J. F. Locking down the Electronic Structure of (Monopyrrolo)Tetrathiafulvalene in [2]Rotaxanes. *Org. Lett.* **2006**, *8* (11), 2205–2208.

(58) Amirthalingam, E. Multi-Functionalization of Micro- and Nanoparticles for Cancer Theranostics, Universitat de Barcelona, 2018.

(59) Stockert, J. C.; Horobin, R. W.; Colombo, L. L.; Blázquez-Castro, A. Tetrazolium Salts and Formazan Products in Cell Biology: Viability Assessment, Fluorescence Imaging, and Labeling Perspectives. *Acta Histochem.* **2018**, *120* (3), 159–167.

(60) Ayala, A.; Muñoz, M. F.; Argüelles, S. Lipid Peroxidation: Production, Metabolism, and Signaling Mechanisms of Malondialdehyde and 4-Hydroxy-2-Nonenal. *Oxid. Med. Cell. Longev.* **2014**, *2014*, 1–31.

(61) Farmer, E. E.; Mueller, M. J. ROS-Mediated Lipid Peroxidation and RES-Activated Signaling. *Annu. Rev. Plant Biol.* **2013**, *64*, 429–450.

(62) Havaux, M.; Triantaphylidès, C.; Genty, B. Autoluminescence Imaging: A Non-Invasive Tool for Mapping Oxidative Stress. *Trends Plant Sci.* **2006**, *11* (10), 480–484.

(63) Griess, B.; Tom, E.; Domann, F.; Teoh-Fitzgerald, M. Extracellular Superoxide Dismutase and Its Role in Cancer. *Free Radic. Biol. Med.* **2017**, *112* (3), 464–479.

(64) Attri, P.; Kim, Y. H.; Park, D. H.; Park, J. H.; Hong, Y. J.; Uhm, H. S.; Kim, K. N.; Fridman, A.; Choi, E. H.

Generation Mechanism of Hydroxyl Radical Species and Its Lifetime Prediction during the Plasma-Initiated Ultraviolet (UV) Photolysis. *Sci. Rep.* **2015**, *5*, 1–8.

(65) Croissant, J. G.; Brinker, C. J. *Biodegradable Silica-Based Nanoparticles: Dissolution Kinetics and Selective Bond Cleavage*, 1st ed.; Elsevier Inc., 2018; Vol. 43.

(66) Lin, Y.-K.; Huang, Z.-R.; Zhuo, R.-Z.; Fang, J.-Y. Combination of Calcipotriol and Methotrexate in Nanostructured Lipid Carriers for Topical Delivery. *Int. J. Nanomedicine* **2010**, *5*, 117–128.

(67) Olson, M. A.; Coskun, A.; Klajn, R.; Fang, L.; Dey, S. K.; Browne, K. P.; Grzybowski, B. A.; Stoddart, J. F. Assembly of Polygonal Nanoparticle Clusters Directed by Reversible Noncovalent Bonding Interactions. *Nano Lett.* **2009**, *9* (9), 3185–3190.

(68) Wu, Y.; Zhou, J.; Phelan, B. T.; Mauck, C. M.; Stoddart, J. F.; Young, R. M.; Wasielewski, M. R. Probing Distance Dependent Charge-Transfer Character in Excimers of Extended Viologen Cyclophanes Using Femtosecond Vibrational Spectroscopy. **2017**.